

# The early X-ray emission from GRBs

P.T. O'Brien<sup>1</sup>, R. Willingale<sup>1</sup>, J. Osborne<sup>1</sup>, M.R. Goad<sup>1</sup>, K.L. Page<sup>1</sup>, S. Vaughan<sup>1</sup>, E. Rol<sup>1</sup>,  
A. Beardmore<sup>1</sup>, O. Godet<sup>1</sup>, C.P. Hurkett<sup>1</sup>, A. Wells<sup>1</sup>, B. Zhang<sup>2</sup>, S. Kobayashi<sup>3</sup>, D.N.  
Burrows<sup>4</sup>, J.A. Nousek<sup>4</sup>, J.A. Kennea<sup>4</sup>, A. Falcone<sup>4</sup>, D. Grupe<sup>4</sup>, N. Gehrels<sup>5</sup>, S. Barthelmy<sup>5</sup>,  
J. Cannizzo<sup>5,6</sup>, J. Cummings<sup>5,7</sup>, J.E. Hill<sup>5,8</sup>, H. Krimm<sup>5,8</sup>, G. Chincarini<sup>9,10</sup>, G. Tagliaferri<sup>9</sup>,  
S. Campana<sup>9</sup>, A. Moretti<sup>9</sup>, P. Giommi<sup>11</sup>, M. Perri<sup>11</sup>, V. Mangano<sup>12</sup>, V. LaParola<sup>12</sup>

## ABSTRACT

We present observations of the early X-ray emission for a sample of 40 gamma-ray bursts (GRBs) obtained using the *Swift* satellite for which the narrow-field instruments were pointed at the burst within 10 minutes of the trigger. Using data from the Burst Alert and X-Ray Telescopes, we show that the X-ray light curve can be well described by an exponential that relaxes into a power law, often with flares superimposed. The transition time between the exponential and the power law provides a physically defined timescale for the burst duration. In most bursts the power law breaks to a shallower decay within the first hour, and a

---

<sup>1</sup>Department of Physics & Astronomy, University of Leicester, Leicester LE1 7RH, UK

<sup>2</sup>Department of Physics, University of Nevada, Las Vegas, NV 89154

<sup>3</sup>Astrophysics Research Institute, Liverpool John Moores University, Twelve Quays House, Birkenhead CH41 1LD, UK

<sup>4</sup>Department of Astronomy and Astrophysics, Pennsylvania State University, 525 Davey Laboratory, University Park, PA 16802

<sup>5</sup>NASA/Goddard Space Flight Center, Greenbelt, MD 20771

<sup>6</sup>Joint Center for Astrophysics, University of Maryland, Baltimore County, Baltimore, MD 21250

<sup>7</sup>National Research Council, 2101 Constitution Avenue, Washington, DC 20418

<sup>8</sup>Universities Space Research Association, 10211 Wincopin Circle, Suite 500, Columbia, MD 21044-3432

<sup>9</sup>INAF, Osservatorio Astronomico di Brera, Via E. Bianchi 46, I-23807 Merate (LC), Italy

<sup>10</sup>Università degli Studi di Milano-Bicocca, Dipartimento di Fisica, Piazza delle Scienze 3, I-20126 Milano, Italy

<sup>11</sup>ASI Science Data Center, via G. Galilei, I-00044 Frascati, Italy

<sup>12</sup>INAF, istituto di Astrofisica Spaziale e Fisica Cosmica Sezione di Palermo, Via U. La Malfa 153, I-90146 Palermo, Italy

late emission “hump” is observed which can last for many hours. In other GRBs the hump is weak or absent. The observed variety in the shape of the early X-ray light curve can be explained as a combination of three components: prompt emission from the central engine; afterglow; and the late hump. In this scenario, afterglow emission begins during or soon after the burst and the observed shape of the X-ray light curve depends on the relative strengths of the emission due to the central engine and that of the afterglow. There is a strong correlation such that those GRBs with stronger afterglow components have brighter early optical emission. The late emission hump can have a total fluence equivalent to that of the prompt phase. GRBs with the strongest late humps have weak or no X-ray flares.

*Subject headings:* Gamma Rays: bursts — black hole physics — accretion disks

## 1. Introduction

Gamma-ray bursts (GRBs) are identified as a brief flash of gamma-rays seen at a random location on the sky. For that instant the GRB becomes the intrinsically brightest single object in the Universe. The duration of a GRB in terms of its prompt emission (i.e., the “burst”) is usually defined in terms of the timescale over which 90% of the gamma-rays were detected – the  $T_{90}$  parameter. It is conventional to describe those GRBs for which  $T_{90} > 2\text{s}$  as “long/soft bursts” and those with shorter duration as “short/hard bursts” (e.g. Kouveliotou et al. 1993).

It is now generally accepted that long-duration GRBs result from the death of a rapidly-rotating massive star (Paczynski, 1998; MacFadyen & Woosley, 1999). The stellar core collapses inwards to form a black hole surrounded by an accreting disk or torus. The accreting material liberates gravitational potential energy either in the form of neutrinos or via magneto-hydrodynamic processes. These generate a relativistic jet, oriented along the rotation axis of the stellar core, which eventually escapes the star. The jet contains a relatively modest amount of baryonic material moving at high Lorentz factor.

Prior to the *Swift* era, almost all of our knowledge about the emission from GRBs beyond a few seconds came from the study of long bursts. Short bursts were, quite literally, too short to be localized by observatories prior to *Swift*. The *Swift* satellite (Gehrels et al. 2004) has changed that situation. The data for the first short bursts detected by *Swift* (Gehrels et al. 2005; Barthelmy et al. 2005b; Hjorth et al. 2005; Bloom et al. 2006) strongly support the idea that the gamma-ray emission seen from short GRBs arises from a jet powered by

a merger of two compact objects, most likely two neutron stars or a neutron star and a black hole. The *Swift* data also show that the X-ray emission from some short bursts can be detected long after  $T_{90}$ , allowing for a direct comparison of the early X-ray emission between short and long GRBs. Some short bursts may have collimated flow (e.g. GRB051221A, Burrows et al. 2006) although this is less clear in others (e.g. GRB050724, Barthelmy et al. 2005b).

For both types of GRB, it is thought that the jet flow is inhomogeneous, leading to internal shocks caused by a variable Lorentz factor (Rees & Mészáros 1994; Sari & Piran 1997). These produce the variable gamma-ray emission seen, when viewing within the jet beam, as a GRB. The gamma-ray emission typically lasts a few tens of seconds before fading below detectability with the current generation of gamma-ray instruments, including the *Swift* Burst Alert Telescope (BAT; Barthelmy et al. 2005a). The sensitivity of BAT is a complicated function of burst duration and spectral shape (see Band et al. 2006). In practice the BAT detects bursts with 15–150 keV fluences as low as  $\sim 10^{-8}$  erg cm $^{-2}$ . The *Swift* satellite, however, has the capability to rapidly slew and point its X-ray Telescope (XRT; Burrows et al. 2005b) and Ultraviolet Optical Telescope (UVOT; Roming et al. 2005) at the burst location. The XRT can detect a source at fainter flux levels in the (observed) 0.3–10 keV band than are possible using extrapolated BAT data. For a Crab-like spectrum and a Galactic column of  $1 \times 10^{20}$  cm $^{-2}$  the XRT detects  $\sim 1$  count per 100s for a source with a 0.3–10 keV flux of  $10^{-12}$  erg cm $^{-2}$  s $^{-1}$ . Thus, *Swift* can routinely follow the evolution of the earliest X-ray emission from GRBs with only modest gaps in the observed light curve.

The GRB flux can be represented as a function of time and frequency using a function  $f_\nu \propto \nu^{-\beta} t^{-\alpha}$ , where  $\beta$  is the spectral index and  $\alpha$  is the temporal index<sup>1</sup>. Analysis of some of the first bursts observed with *Swift* shows that the early X-ray light curves are complex. In some cases (e.g. Tagliaferri et al. 2005; Hill et al. 2006; Cusumano et al. 2006; Vaughan et al. 2006a) the early X-ray emission (observed with the XRT within a few hundred seconds of the burst) can decline rapidly in the first few minutes, with  $\alpha \sim 3$  or greater. The light curve can then show a break to a shallower decay component, which we will henceforth refer to as the late emission “hump”. Analysis of GRB samples from the early phase of the *Swift* mission (Nousek et al. 2006) confirm that this pattern of a rapidly decaying light curve followed by a late emission hump is common. However, in some bursts the earliest observed X-ray flux appears to decline relatively slowly ( $\alpha \sim 1$ ) (e.g. Campana et al. 2005; Blustin et al. 2006).

The fading X-ray emission could be due to a number of components, including high-

---

<sup>1</sup>The photon index  $\Gamma$  is related to  $\beta$  by  $\Gamma = \beta + 1$ .

latitude emission from the fading burst (Kumar & Panaitescu 2000), the interaction of the jet with the surroundings — the afterglow emission produced by an external shock (e.g. Mészáros & Rees 1997), and thermal emission from a photosphere around the outflow (e.g. Mészáros & Rees 2000) or from a hot cocoon associated with the jet (e.g. Mészáros & Rees 2001). A significant fraction of GRBs also show X-ray flares (e.g. Burrows et al. 2005a) superimposed on the declining light curves.

If the BAT and the XRT are initially detecting the prompt emission from the jet, the most rapidly-decaying X-ray light curves could be due to viewing photons at high-latitudes (i.e. large angles to the line-of-sight) as the prompt emission fades (Kumar & Panaitescu 2000; Tagliaferri et al. 2005; Nousek et al. 2006; Zhang et al., 2006; Panaitescu et al. 2006). In at least one case (GRB050219a, Tagliaferri et al. 2005), the BAT and XRT light curves do not appear to join and in other cases the observed X-ray rapid decay rate is higher than expected from the high-latitude model (e.g. Vaughan et al. 2006a). Alternatives such as structured jets (e.g. Zhang & Mészáros 2002), multiple jets or patchy jets (e.g. Burrows et al. 2005c) in which we see varying emission as our light cone expands are also possibilities. These models have difficulties, however, explaining those bursts that decline relatively slowly for which other emission components, such as the afterglow, may contribute at the earliest times. Both the rapid-decay and afterglow models have difficulties explaining the late emission hump. This component may be due to forward shock emission, which is refreshed with energy either due to continued emission from the central engine or because the ejecta have a range in initial Lorentz factor (Rees & Mészáros 1998; Sari & Mészáros 2000; Zhang & Mészáros 2001; Nousek et al. 2006; Zhang et al. 2006; Granot & Kumar 2006).

To disentangle the relative contribution of emission from the central engine and that due to afterglow, and hence understand the origin of the early gamma-ray and X-ray emission, requires a systematic analysis of the temporal and spectral properties of a large GRB sample combining data from the BAT and XRT. The previous studies of GRB samples from *Swift* (e.g. Nousek et al. 2006) include a relatively small number of GRBs with early (few minutes from trigger) XRT observations and do not include a combined temporal and spectral analysis of data from the BAT and XRT. The aim of this paper is to determine the shape of the early X-ray light curve and spectrum for a large sample of GRBs for which observations were obtained early with the *Swift* narrow field telescopes. We use the combined BAT and XRT data to determine whether an extrapolation of the early gamma-ray emission detected by the BAT joins smoothly to that seen by the XRT, whether or not there is always a rapid decline phase seen by either instrument and to investigate the relative importance of emission from the central engine and the afterglow.

Our GRB sample is summarized in section 2. The analyses of the BAT and XRT data are presented in sections 3 and 4 and we explain how the data from the two instruments were combined in section 5. The observed temporal and spectral shapes are presented in section 6. In section 7 we describe a light curve fitting technique which we use to study the various components contributing to the early X-ray emission. The discussion and conclusions are given in sections 8 and 9 respectively.

## 2. GRB sample

Our initial GRB list of potential bursts comprised those detected by *Swift* prior to 2005 October 1 for which *Swift* slewed to point its narrow-field instruments within 10 minutes of the burst trigger time. In the majority of cases the XRT observations started within 2 minutes. Of the 45 such GRBs, we excluded 5 from our detailed analysis: GRB050117A ( $T_{90} = 167\text{s}$ ; Hill et al. 2006), GRB050509B ( $T_{90} = 0.04\text{s}$ ; Gehrels et al. 2005), GRB050815 ( $T_{90} = 2.6\text{s}$ ), GRB050906 ( $T_{90} = 0.02\text{s}$ ) and GRB050925 ( $T_{90} = 0.01\text{s}$ ). Four of these are short and faint, and as a result insufficient X-ray photons were obtained in the first hour with which to accurately constrain the early X-ray spectral and temporal indices. Only one of the excluded GRBs is a long burst (GRB050117A). In this case the XRT obtained few data due to it being observed initially whilst *Swift* was in the South Atlantic Anomaly. Allowing for these problems, these bursts are consistent with the sample studied here.

The 40 remaining GRBs form our sample and are listed in Table 1. Following convention, the bursts are named as GRB-year-month-day with a following letter (A, B, C ...) if multiple bursts were detected on that day. We adopt the usual  $T_{90}$  convention for long and short bursts, but note that the assignment does depend on the detector sensitivity and bandpass. We use the 15–150 keV band. We include 2 bursts — GRB050724 and GRB050813 — which we classify as short bursts to see how they compare. GRB050724 formally has a  $T_{90} > 2\text{s}$  in the BAT, but this is due to a long, fairly soft X-ray tail of emission (Barthelmy et al. 2005b). It would have appeared to be a short burst with  $T_{90} \sim 0.4\text{s}$  in the BATSE/CGRO instrument (Fishman et al. 1994).

## 3. BAT analysis

All of the GRBs discussed in this paper were detected by the *Swift* Burst Alert Telescope. Once triggered, the BAT determines if there is a new point source, and the *Swift* figure-of-merit processor then computes whether this source can be observed immediately (i.e., is

unconstrained by the Earth, Moon or Sun). If so, the satellite is commanded to slew to put the target in the field of view of the narrow-field instruments. The BAT continues to observe during the slew, providing an uninterrupted light curve.

The BAT data for the GRB sample were processed using the standard BAT analysis software (*Swift* software v. 2.0) as described in the BAT Ground Analysis Software Manual (Krimm, Parsons & Markwardt 2004) and then light curves and spectra were extracted over 15–150 keV, correcting the response matrix during slews<sup>2</sup>. The derived values of  $T_{90}$  and  $T_{50}$  are given in Table 1, along with the mean fluxes and spectral indices derived from fitting single power laws ( $N_{\text{ph}}(E) \propto E^{-\Gamma_b}$ ) over the period corresponding to  $T_{90}$ . Thus, the spectral properties are averages over  $T_{90}$ . Throughout this paper all quoted errors on fit parameters correspond to 90% confidence for a single parameter (i.e.  $\Delta\chi^2 = 2.706$ ). **XSPEC v11.3** (Arnaud 1996) was used to fit the BAT and XRT spectra.

A single power law provides a statistically acceptable fit to the BAT data in most cases. The four GRBs for which a cut-off power law model ( $N(E) \propto E^{-\Gamma_{bc}} \exp(-E/E_{\text{cut}})$ ) provides a significantly better fit (at  $> 99\%$  confidence) with a well determined  $E_{\text{cut}}$  are noted in Table 2, which gives the low energy spectral indices ( $\beta_{bc} = \Gamma_{bc} - 1$ ) and the e-folding energies of the exponential cut off ( $E_{\text{cut}}$ ). The  $T_{90}$  and  $\beta_b$  distributions are not significantly different from those found for previous GRB samples.

#### 4. XRT analysis

The XRT observations used here began at the times given in column 2 of Table 3. These times are relative to the GRB trigger time determined by the BAT. The XRT observations incorporate data taken using the various operating modes of the instrument (see Hill et al. 2004) and were corrected for pile-up where appropriate using the method described in Nousek et al. (2006). The bulk of the XRT data presented here were obtained using Windowed Timing (WT) or Photon Counting (PC) modes (event grades 0–2 and 0–12 respectively). The XRT data were processed using **xrtpipeline v0.8.8** into filtered event lists which were then used to extract spectra and light curves for the 0.3–10 keV energy range.

The X-ray light curves are generally complex, often with “flares” and frequent changes in temporal slope which can occur over short time intervals, particularly at early times. As an initial simple parameterisation, we have fitted the XRT light curves obtained over the first few orbits with a broken power law model with flux  $\propto (t - t_0)^{-\alpha_1}$  before some break

---

<sup>2</sup><http://swift.gsfc.nasa.gov/docs/swift/analysis/>

time,  $t_{\text{break}}$ , and  $\propto (t - t_0)^{-\alpha_2}$  after the break. This function quantifies the early decay rate and any late emission hump. The temporal decay slopes and the break times are given in Table 3 and were determined using the BAT trigger time as  $t_0$ . This time corresponds to the start of the first foreground interval for which the BAT was able to locate a point source. This may not coincide with the initial rise in count rate.

For GRB50319 automatic triggering was disabled during the start of the burst as *Swift* was slewing, and the GRB actually started some 135s before the BAT trigger (Cusumano et al. 2006). For that GRB we include all data following the onset of the burst determined from the pre- and post-BAT-trigger light curve using the  $t_0$  from Cusumano et al. (2006).

We have visually judged when to exclude flares and short-duration changes of slope to provide the early XRT decay index ( $\alpha_1$ ). We stress, however, that such a representation is indicative of, rather than completely representative of, the complex X-ray light curves. We return to this issue in section 7 where we adopt a more automatic approach to parameterise the light curve and to select  $t_0$ . Unlike Nousek et al. (2006), we do not distinguish in Table 3 between those bursts that decay rapidly or slowly in the earliest XRT observations. That is, we do not group bursts into decay phases based on assuming an early steep decay phase is always visible — we show later that this is not always the case. Rather the values of  $\alpha_1$  and  $\alpha_2$  given in Table 3 correspond to the decay rates either side of the first clearly observed temporal break in the XRT light curve. In some bursts no break in X-ray temporal slope is clearly detected using the XRT data alone, in which case only  $\alpha_1$  is tabulated. The mean value of  $\alpha_1$  is 2.45 with a standard deviation of 1.55.

X-ray spectra were obtained from the early data and fitted with a single power law model, allowing for both Galactic (Dickey & Lockman 1990) and intrinsic absorption using the **wabs** model in **XSPEC**. The default cross sections and abundances were used (Morrison & McCammon 1983; Andres & Ebihara 1982). The derived early XRT spectral indices ( $\beta_x$ ) and absorbing columns are given in Table 3. In general little evidence is found for spectral evolution across early temporal breaks (see also Nousek et al. 2006) but where evolution is seen the XRT spectrum tends to get harder. Aside from GRB 050525A where photodiode mode data were used, the data used for the XRT spectra were obtained from the first orbit of WT data (pre-break for GRB 050219A and pre-flare for GRB 050502B) or the first orbit of PC mode data (GRBs 050126, 050128, 050315, 050319 (pre-break), 050401, 050406 (pre-flare), 050412, 050416A (pre-break), 050607, 050813, 050826, 050908 and 050916).

A majority of the GRBs show evidence for excess absorption above the Galactic column at the  $> 99\%$  confidence level. The excesses given in Table 3 have been converted to rest-frame absorbing columns for those GRBs for which a redshift is known. For the bursts with redshifts, the intrinsic column ranges from  $2 \times 10^{21} \text{ cm}^{-2}$  up to  $3.5 \times 10^{22} \text{ cm}^{-2}$  consistent

with the idea that these GRBs occur in a molecular cloud environment (Reichart & Price 2002; Campana et al. 2006).

## 5. Combining the BAT and XRT light curves

As the BAT and XRT data cover different energy bands and seldom overlap in time, to compare them the data for one instrument must be extrapolated into the bandpass of the other. We have chosen to use the 0.3–10 keV bandpass to determine fluxes as the bulk of the temporal data, particularly during the decline, were obtained using the XRT.

In Fig. 1 we plot of the distribution of  $\beta_b$  and  $\beta_x$ . The solid line shows equality of spectral index. There is a trend such that the early XRT data are fitted by a systematically softer power law than the BAT data (i.e.  $\beta_x > \beta_b$ ). The mean values of  $\beta_b$  (using single power law fits) and  $\beta_x$  are 0.74 and 1.16 with standard deviations of 0.50 and 0.76 respectively.

The spectral trend is in the same sense as the known tendency for GRB prompt gamma-ray emission to become softer at later times (Ford et al. 1995). We have used this tendency when combining the BAT and XRT data to form the unabsorbed, 0.3–10 keV flux light curves shown in Fig. 2. These light curves were constructed by: (a) converting the XRT count rates into unabsorbed fluxes using the power law model parameters as given in Table 3; and (b) converting the BAT 15–150 keV count rates into unabsorbed 0.3–10 keV fluxes by extrapolating the BAT data to the XRT band using a power law model with a spectral index which is the mean of the XRT and best-fit BAT spectral indices. This method was used for all bursts except GRB050714B for which the early XRT spectral index is exceptionally soft and appears to evolve rapidly (Levan et al. 2006). For GRB050714B we have used the  $\beta_b$  from Table 1 to convert BAT counts to flux. It should be noted that in Fig. 2 the time axis is limited at 10<sup>5</sup>s to emphasise the early part of the light curve. For some bursts observations continued beyond that time and all data were included when performing the temporal fits given in Table 3 and when analysing the data further in section 6.

The observed spectra for the BAT and XRT and the ratio of the spectra to a power law are also shown in Fig. 2. In these plots the relative normalisations of the XRT and BAT data were allowed to be free parameters while the spectral index was frozen at the single power law value obtained for the BAT. The residuals illustrate the generally softer X-ray spectrum seen by the XRT compared to the BAT.



## 6. The observed early temporal and spectral shape

The observed GRB properties for the *Swift* sample in terms of spectral hardness and duration indicate that it is broadly representative of the GRB population observed by BATSE (Kouveliotou et al. 1993; Berger et al. 2005). The difference is that *Swift* provides X-ray data over a much longer time interval than previous missions and can detect GRBs with lower mean fluxes. Combining the BAT and XRT data also allows for a view of the prompt phase of GRB emission with little or no temporal gap.

Although GRB light curves can have considerable structure superimposed on the overall decline (see below) following the initial burst, the data shown in Fig. 2 strongly suggest that there is no discontinuity between the emission seen by the BAT and the later emission seen by the XRT. In every case where the burst was long enough for the XRT to start observing before the end of  $T_{90}$  the BAT and XRT light curves join smoothly. For those GRBs where there is a temporal gap of only a few tens of seconds the light curves can be smoothly extrapolated to join. For those GRBs with a short  $T_{90}$  the extrapolation is naturally over a longer time, but even for these cases the BAT and XRT data appear to join up.

The only cases for which there is a temporal gap and where the extrapolated BAT light curve may not agree with the XRT are GRB050219A and possibly GRB050525A. For GRB050219A, allowing for the spectral evolution observed by the BAT does not resolve this problem (Tagliaferri et al. 2005; Goad et al. 2005). The apparent discontinuity could, however, be due to an X-ray flare in this burst around 90s after the trigger. As noted above, the presence of late X-ray flares in GRBs is now known to be common. For GRB050525A, which like GRB050219A is best-fitted by a cut-off power law in the BAT, some spectral evolution or an early break in the light curve similar to that in GRB050713A could be responsible.

For the 5 bursts excluded from detailed analysis, no counts were detected with the XRT for GRB050906 and GRB050925. The combined BAT+XRT X-ray light curve for GRB050815 suggests it declined rapidly before 100s and then decayed more slowly until a few thousand seconds, similar to the X-ray decay seen in GRB050509B (Gehrels et al. 2005). GRB050117A, which was observed while *Swift* was in the South Atlantic Anomaly, appears to display a rapid decline after the prompt phase followed by a shallow decline until 10ks (Hill et al. 2006), and hence is consistent with the behaviour of the rest of the long bursts in the sample.

As GRBs are, by their very nature, transient, all bursts show a decline following the prompt phase. The rate of decline, and how long it lasts, varies. This is indicated by the large standard deviation in  $\alpha_1$  noted above. Visual inspection of the light curves show that

some two-thirds of the GRBs have X-ray light curves that show an early more rapid phase of decline which then breaks to a late emission hump. This temporal break is observed to occur over a wide range of times but is usually within the first hour, and is clearly not a jet break. The remaining GRBs seem to have a continuous decline. Those which do not seem to flatten have only a single ( $\alpha_1$ ) decay index given in Table 3. The mean value of the X-ray spectral index is not different between those GRBs with or without a rapid decay phase.

Around half of the GRBs appear to show late ( $t > T_{90}$ ) X-ray flares. These include GRB050406, 050502B, 050607, 050713A, 050714B, 050716, 050724, 050801, 050813, 050820A, 050822, 050904, 050908, 050916 and 050922B. A few others (e.g. GRB050219A, 050319, 050802, 050915A) may have flares at the start of the XRT observation. Most of these flares contain the equivalent of 10% or less of the prompt fluence, but in a few cases have  $> 50\%$  (e.g. GRB050502B (Burrows et al. 2005b) and GRB050820A (Osborne et al. 2006)). There is no significant difference between the rate of flares for those GRBs with or without a very steep decline X-ray phase.

Neither  $\alpha_1$  nor  $\beta_x$  are significantly correlated with  $T_{90}$ . There is a weak correlation between  $\alpha_1$  and  $\beta_x$  (Fig. 3; Spearman’s rank correlation coefficient  $r = 0.30$ , significant at 95%), although this depends on including GRB050714B. In contrast, over a wide range in  $\alpha_1$ , there is a very strong correlation between  $(\alpha_1 - \beta_x)$  and  $\alpha_1$  (Fig. 4,  $r = 0.89$ , significant at  $\gg 99.9\%$ ). The sense of the correlation is such that those GRBs with shallower temporal decays have a smaller difference between their temporal and spectral indices. This correlation is consistent with no strong dependence of  $\beta_x$  on  $\alpha_1$ .

It has been suggested (e.g. Nousek et al. 2006; Zhang et al. 2006) that the steeply declining early X-ray emission seen in early XRT observations can be interpreted in terms of “high latitude” emission (Kumar & Panaitescu 2000). In this model if the physical process producing the X-ray emission (such as internal shock activity) stops, the observed emission will continue for a short time as the observer will continue to see emission from those parts of the jet which are off the immediate line of sight. Thus emission at angles  $\theta$  from the line of sight which are in excess of  $\theta = \Gamma_{jet}^{-1}$  will start to dominate the observed emission, where  $\Gamma_{jet}$  is the jet Lorentz factor. For a uniform surface brightness jet, the energy in some bandpass will fall as  $t^{-\beta-2}$  where the spectrum is  $\propto \nu^{-\beta}$  (Kumar & Panaitescu 2000). In terms of spectral index, this model predicts a relation such that  $\alpha - \beta = 2$  for the early, rapidly declining part of the temporal decay. It is possible to get a shallower decay if viewing a structured-jet off-axis (Dyks, Zhang & Fan 2006) although the general trend is similar to the standard high-latitude model.

From Fig. 4, for the entire sample  $\alpha_1$  appears to be largely independent of  $\beta_x$  or at least is not simply related. This is inconsistent with the concept that the early X-ray emission is

usually dominated by high latitude emission in a uniform jet. An alternative explanation for the early X-ray emission GRBs is afterglow emission, but this also predicts a specific relation between the spectral and temporal indices, as discussed below. Overall, the data shown in Fig. 4 suggest that no single model will explain all of the bursts.

To try and force a fit with a particular model we could adjust the start time of the time series,  $t_0$ , to some point in the prompt light curve such that the relation between  $\alpha$  and  $\beta$  fits a particular model and is not simply defined by the BAT trigger time.. For example, moving forwards to a late flare, if one is observed, or earlier to a visually estimated start time. Rather than adopt such a subjective and model dependent approach, we have developed a method to automatically align the light curves. In sections 7 and 8 we use this technique to investigate the early X-ray light curve in GRBs and hence determine the contribution of likely emission components.

## 7. The global GRB X-ray decay curve

In order to compare light curves for different GRBs and to study the different phases of the X-ray emission, we have developed a procedure to fit light curves. This procedure, described below, attempts to provide a best fit to the “global light curve” for all our GRBs, assuming there is a generic pattern to their behaviour. It uses information from the combined BAT+XRT flux light curve for each burst and can adjust the start of the time series (i.e. move  $t_0$ ) and the temporal scale of the decay, while also allowing for deviations from the global decay (termed flares and humps below) to derive a standard set of parameters for each burst.

An average X-ray decay curve expressed by  $\log(\text{time})$  as a function of  $\log(\text{flux})$ ,  $\tau(F)$ , and  $\log(\text{flux})$  as a function of  $\log(\text{time})$ ,  $F(\tau)$ , was derived by taking the sum of scaled versions of each of the individual light curves,  $f_i(t_i)$ , where  $t_i$  is approximately the time since the largest/latest peak in the BAT light curve. The data points were transformed to normalised  $\log(\text{flux})$ ,  $F_i = \log_{10}(f_i/f_d)$ , and  $\log(\text{time})$  delay values,  $\tau_i = \alpha_d \log_{10}(t_i - t_d) - \tau_d$ . Four decay parameters (suffix  $d$ ) specify the transformation for each GRB:  $f_d$ , the mean prompt flux;  $t_d$ , the start of the decay;  $\tau_d$ , a time scaling; and  $\alpha_d$ , a stretching or compression of time. The flux scaling is a simple linear shift in the log-scale and does not involve any stretching or compression of one GRB with respect to another. Under the transformation all the light curves conform to an approximately universal behaviour with an initial exponential decline  $\propto \exp(-t/t_c)$  followed by a power law decay  $\propto t^{-\alpha_0}$ .

The transition between the two decay phases occurs when the exponential and power

law functions and their first derivatives are equal, and is given for the average decay curve by  $t_0 = t_c \alpha_0$  ( $\tau_0 = 1.7$ ). Adopting this transition, for each GRB we define the division between the prompt and power law decay phases to be  $\tau_0$ , corresponding to a prompt time  $T_p = 10^{(\tau_0 + \tau_d)/\alpha_d}$  seconds. This definition of  $T_p$  provides us with an alternative estimate of the duration of each burst which depends on the physical shape of the light curve, takes into account the data from both the BAT and the XRT and is not bound by the sensitivity of either instrument. It does depend on the chosen energy band and method used to extrapolate. Depending on the particular characteristics of the burst,  $T_p$  can be similar to, greater than or smaller than  $T_{90}$ .

The best fit  $f_d$ ,  $t_d$ ,  $\alpha_d$  and  $\tau_d$  for each GRB were found using a least squares iteration procedure. Initial values for these parameters were chosen by visual inspection of the light curves and a first guess for the average decay curve,  $F_{av}(\tau_{av})$ , was set up using nominal values for  $t_c$  and  $\alpha_0$ . The zero time  $t_d$  was initially set to the position of the largest peak for each burst. The flux was normalised by calculating  $f_d$  which minimized the square difference between the average flux curve and each data point,  $\sigma_f = \sum (F_i - F_{av}(\tau_i))^2$ , summing over all data points in the prompt phase  $\tau < \tau_0$ . In order to perform the least squares fitting in the time domain, each light curve was binned as temporal delay values over a set of bins in  $F$  (rather than averaging the flux values over time bins) and the average temporal delay for each flux bin was calculated. The temporal parameters  $\tau_d$ ,  $\alpha_d$  and  $t_d$  were updated minimizing  $\sigma_\tau = \sum (\tau_{av}(F_i) - \tau_i)^2$  summing over all the measured values at different flux levels for  $\tau_0 < \tau < \tau_h$  where  $\tau_h = 3.5$ . The upper limit  $\tau_h$  is set to take into account the late emission hump. Bright flares in the decay phase were excluded during the minimization procedure.

At the end of each iteration the  $\alpha_d$  values were scaled so that the mean over all the GRBs was unity and the  $\tau_d$  values were offset so that the mean was zero. This ensures that  $\tau$  has units of  $\log_{10}(seconds)$ . Using the updated parameter values a new best guess at the average decay curve was calculated summing over all 40 GRBs. The iteration was stopped when the changes in the parameters were sufficiently small. The average decay curve derived from 40 GRBs and all the measured flux values from the BAT and XRT (4569 measurements) are shown in Fig. 5. The values of  $T_p$  are given in Table 4. An example of the transformation for one burst (GRB 050819) is shown in Fig. 6. This figure shows that  $t_d$  is moving the zero time (hence some of the early prompt points are before the start time in transformed space). Then  $\tau_d$  and  $\alpha_d$  rescale the units of logarithmic time.

The average decay curve relaxes into a power law with a decay index  $\alpha_0 = 2.1$  found by linear regression on the average decay curve for  $\tau_0 < \tau < 3.0$ . This power law fit is shown as a dashed line in Fig. 5. The fitting procedure results in those GRBs which follow a fairly

continuous decay lying close to the power law. At  $\tau \sim 3$  the average decay curve starts to rise above the power law decay in the majority of bursts. This is the start of the late emission hump, which has a large observed variety in strength which we parameterize below. The range in hump strength results in the somewhat jagged appearance of the average decay curve for  $\tau > 3.5$ .

GRB050730 falls below the average decay curve at  $\tau \sim 2.5$ . This object has the largest value of  $T_p$  (373 seconds) and a decay which gets much steeper at  $\tau \approx 2.5$ . The last few data points for this source can be seen below the bulk of the data on Fig. 5. For GRB050319 the fit procedure prefers a fit using the first (larger) peak in the BAT light curve as the burst and treats the second, later peak as a flare. If we force the procedure to adopt a  $t_0$  just before the second lower-flux peak we derive a very steep early decay index ( $\sim 5$ ) but get a significantly worse fit to the rest of the light curve.

The distribution of  $\log_{10}(T_p/T_{90})$  as a function of  $\log_{10}(T_{90})$  is shown in Fig. 7. For almost all bursts  $T_p$  is comparable to or somewhat larger than  $T_{90}$  as expected. For GRB050421 it is a factor of 17 larger. For this burst, if the BAT data beyond the  $T_{90}$  period are binned up a long tail extending to the start of the XRT observations can be seen (Godet et al. 2006). For GRB050820A  $T_p$  is a factor of 12 smaller than  $T_{90}$ . There is a very bright second burst/flare seen from this object which was excluded from the average curve fitting but which is included when calculating the BAT  $T_{90}$  estimate. This second event is brighter than the first (Osborne et al. 2006).

The early light curves are plotted in linear time relative to  $T_p$ ,  $(t - t_d)/T_p$  in Fig. 8. The peaks (global maximum flux measurements for each burst) are shown as filled circles. The notable exception is GRB050422 (Beardmore et al. 2006) for which the peak occurs at  $(t - t_d)/T_p \approx 0.6$ . For this burst a large late flare is seen in the BAT followed by a rapid decay. In this case the fitting procedure has chosen  $t_d$  such that the peak falls at the centre of the  $T_p$  window. GRB050922B also has a bright flare late in the BAT light curve giving a peak at  $(t - t_d)/T_p \approx 0.35$ . Because the peaks are clustered around zero we can be confident that any temporal indices derived for the subsequent decays relate to the appropriate maximum in the light curve. The line connecting the open circles is a linear fit to the average decay curve. Since this is a linear-log plot this represents an exponential decay from the initial peak value. The time constant for the exponential decay is  $t_c = 0.47T_p$  which is equivalent to  $\tau = 1.4$  on Fig. 5. The curved solid line is the extrapolated power law.

The initial temporal decay index for individual GRBs can be calculated by multiplying  $\alpha_0$  by the best fit  $\alpha_d$ . GRBs with  $\alpha_d > 1$  have decays steeper than average and those with  $\alpha_d < 1$  shallower. In Fig. 9 we plot  $\alpha_0\alpha_d$  versus the  $\alpha_1$  parameter derived from the XRT light curves (from Table 3). Using the least squares fit to the average decay curve has reduced the

spread of decay index values and in general the  $\alpha_0\alpha_d$  are somewhat smaller than  $\alpha_1$ . The  $\alpha_0\alpha_d$  are based on all the available data from both the BAT and XRT and are expected to be a more robust estimate of the global average. In contrast  $\alpha_1$  provides a snap-shot of a particular (often rather short) section in the overall light-curve and were derived using the BAT trigger time.

Many of the GRBs have excess flux over and above the average power law decay. In order to quantify this we have calculated the average difference,  $\sum(F_i - F_{pl}(\tau_i))/n_r$ , between the measured data and the average power law decay  $F_{pl}(\tau)$  over the ranges  $\tau_0 < \tau < \tau_h$ , giving  $\Delta_F$ , and over  $\tau_h < \tau < 10$ , giving  $\Delta_H$ , summing over the  $n_r$  data points which fall within each range. Thus  $\Delta_F$  and  $\Delta_H$  provide a measure of the flaring activity in the power law decay phase and the strength of the late emission hump. The mean differences are calculated in  $\log_{10}(\text{flux})$  and therefore represent  $\log_{10}$  of a multiplicative factor over and above (or below if negative) the average power law decay curve. Two bursts, GRB050202B and GRB050916 have a flare at  $\tau > \tau_h$  which is included in their  $\Delta_H$  calculation.

The values of  $\Delta_H$  plotted against  $\Delta_F$  are shown in Fig. 10. There is no correlation between these values. The GRBs in each quadrant are shown as filled (black) circles (no significant flares or hump), filled (green) squares (flares but no hump), filled (blue) stars (flares and hump) and filled (red) triangles (hump but no flares). The objects plotted as open circles (with  $\Delta_H = 0$ ) are those for which there are no late data. In most cases this is because the afterglow was too faint to detect in the XRT and so a value of zero has been taken as a reasonable estimate of  $\Delta_H$  for these objects.

The values of  $\alpha_0\alpha_d$ ,  $\Delta_F$ ,  $\Delta_H$ ,  $T_p$  and  $\alpha_f$  (defined below) for the GRB sample are given in Table 4. Fig. 11 shows four examples of scaled GRB light curves plotted with the average decay curve. These examples illustrate GRBs with a range of early decay rates and flares and humps of different strengths.

## 8. Discussion

The procedure which calculates the average X-ray decay curve generates several parameters for each GRB:  $f_d$ , the mean prompt flux level;  $T_p$ , the duration of the prompt emission;  $\alpha_0\alpha_d$ , the temporal decay index of the initial decay;  $\Delta_F$ , a measure of the level of flaring activity during the initial power law decay; and  $\Delta_H$ , a measure of the size of the late emission hump after the initial power law decay.

The distributions of  $\alpha_0\alpha_d$  and  $\log_{10}(T_p)$  are shown in Fig. 12. There is no correlation between the duration of the burst and the initial decay index. However, the bursts clearly

cluster according to the relative prominence of flares or humps.

As shown in Fig. 12, the majority of the sample are bunched in the range  $4.5 < T_p < 140$  seconds and  $0.9 < \alpha_0\alpha_d < 3.2$ . GRB050730 ( $T_p = 157$ ,  $\alpha_0\alpha_d = 0.85$ ) and GRB050904 ( $T_p = 282$ ,  $\alpha_0\alpha_d = 1.39$ ), both high redshift bursts, are somewhat isolated from the main population with relatively long decays and low temporal decay indices. GRB050813, a short burst, has the smallest  $T_p$ .

We can use the values of  $\alpha_0\alpha_d$  to test the high latitude and other emission models. The correlation of  $\alpha_0\alpha_d$  with  $\beta$ , the average of the BAT and XRT spectral indices (except for GRB050714B for which  $\beta_b$  was used), is shown in Fig. 13. There is a correlation (correlation coefficient 0.53, significant at 99%) between the decay index and the spectral index for all the data plotted, but the relation between  $\alpha_0\alpha_d$  and  $\beta$  does not match the high latitude model prediction, shown by the solid line, and there is clearly very significant scatter. This correlation, and other significant correlations discussed in this paper, are summarized in Table 5.

In principle, the relationship between the temporal decay index and spectral index has two components such that  $\alpha = \alpha_\nu\beta + \alpha_f$ . The coefficient  $\alpha_\nu$  arises from the redshift of the peak of the spectral distribution of the synchrotron emission as a function of time, while  $\alpha_f$  arises from the temporal decay in the peak flux value of the same spectral distribution. The solid line in Fig. 13 shows the expected relationship for the high latitude model (Kumar & Panaitescu 2000) with  $\alpha_\nu = 1$  and  $\alpha_f = 2$ . The dashed line shows the relationship expected from an afterglow expanding into a constant density ISM observed at a frequency below the cooling break ( $\nu_x < \nu_c$ ) and before a jet break, with  $\alpha_\nu = 3/2$  and  $\alpha_f = 0$  (Sari, Piran & Narayan 1998). We will use this as our afterglow model. If  $\nu_x > \nu_c$  then  $\alpha_\nu$  is unchanged and  $\alpha_f = -0.5$ ; this is plotted as a dot-dashed line on Fig. 13. All of the GRBs lie on or above these afterglow lines. We adopt the ISM model as the light curves for most GRBs appear consistent with the presence of a fairly constant density medium (e.g. Panaitescu & Kumar 2002, Yost et al. 2003, Blustin et al. 2006). Using a wind model would not change the conclusions below.

The best fit correlation for all the bursts shown in Fig. 13 has  $\alpha_\nu = 1.8$  and  $\alpha_f = 0.53$ , which is a poor fit to either model. The best fit correlation (correlation coefficient 0.66, significant at  $\gg 99.9\%$ ) for those bursts which lie below the high latitude line is shown as the dotted line. For these objects  $\alpha_\nu = 1.3$ , close to the average of the high latitude and afterglow models, but the intercept is  $\alpha_f = 0.75$ , indicating that the peak flux is not decaying as fast as expected for the high latitude emission.

Of the 5 GRBs which lie significantly above the high latitude prediction in Fig. 13, 4

have the most significant late humps. The other is GRB050421 for which we have no late data as it quickly faded below detectability (Godet et al. 2006). Aside from GRB050421, 3 out of 4 have  $\alpha_0\alpha_d > 3$  which is formally the maximum that the high latitude model allows (Kumar & Panaitescu 2000). One of these, GRB050422, has a large late flare in the BAT which is placed at  $(t - t_d)/T_p \approx 0.6$  (see Fig. 8). If this peak is pushed nearer to the temporal origin then the decay index becomes smaller ( $\approx 3.2$ , Beardmore et al. 2006) but if we do this the overall fit to the average decay profile is very poor. For the other two, GRB050315 and GRB050915A, the most significant peak in the BAT light curve is close to the temporal origin and the overall fit to the average profile is excellent. The BAT light curve for GRB050315 is dominated by a single flare and Vaughan et al. (2006a) give a similarly high decay index value ( $\alpha_1 \sim 5$ ). The large majority of GRBs lie below the high latitude prediction. For these it is likely that we are seeing a combination of high latitude prompt emission and conventional, pre-jet-break afterglow.

The lines shown on Fig. 13 are just some of a family of curves with the form  $\alpha = \alpha_\nu\beta + \alpha_f$ , each with a unique intercept  $\alpha_f$  and corresponding gradient  $\alpha_\nu$ . Assuming the emission from each GRB corresponds to a combination of the high-latitude and afterglow models shown as the solid and dashed lines (discussed above), we can parameterise each of the GRBs with an intercept  $\alpha_f = (\alpha_0\alpha_d - 3\beta/2)/(1 - \beta/4)$  which is given in Table 4. If objects have  $\alpha_f \sim 0$  they conform to the prediction of the afterglow model and if  $\alpha_f \sim 2$  they conform to the prediction of the high latitude model. Thus  $\alpha_f$  serves as a measure of the combination of these 2 components.

We might expect those GRBs which have smaller  $\alpha_f$  (more afterglow dominated) to be more likely to have an early optical detection. Using UVOT data<sup>3</sup> to quantify the early optical brightness, the data support such a relationship. Of our sample, 33 GRBs have UVOT observations in the first 10 minutes, of which 11 are detected in V. All of these 11 have  $\alpha_f < 0.85$ . In contrast, of the 22 GRBs with upper limits (typically  $V > 19$ ), 19 have  $\alpha_f > 0.85$ . The likelihood of a UVOT detection also correlates with  $\alpha_0\alpha_d$ , such that GRBs with  $\alpha_0\alpha_d < 2$  are four times more likely to have been detected.

It is clear from Fig. 13 that the decay index,  $\alpha_0\alpha_d$ , correlates with the strength of flares and humps, i.e. the location of a burst in this figure depends on its location in Fig. 10. The bursts with the most significant humps do not have large X-ray flares but they do have steep decays and straddle the high latitude line in Fig. 13. The bursts with no significant flares or humps all lie below the high latitude line in the bottom-left part of Fig. 13. In the context of the ISM afterglow model, for these GRBs the implied electron energy index,  $p \sim 2 - 2.5$ . For

---

<sup>3</sup>[http://swift.gsfc.nasa.gov/docs/swift/archive/grb\\_table/](http://swift.gsfc.nasa.gov/docs/swift/archive/grb_table/)



the bursts clustering around  $\alpha_0\alpha_d \sim 2.5$  and  $\beta \sim 1.5$ , which appear close to the afterglow lines at the mid-right of Fig. 13, the implied  $p > 3$ .

The late hump starts to appear at  $\tau_h = 3.5$ , which corresponds to a time  $T_h = 10^{(\tau_h + \tau_d)/\alpha_d}$ . The ratio of the prompt time ( $T_p$ ) to this hump time is given by  $\log_{10}(T_p/T_h) = -1.8/\alpha_d$ . We can integrate the light curves to find the fluence for  $t > T_h$ ,  $E_h$ , and compare this with the fluence under the average power law for the same time interval,  $E_{pl}$ . The ratio  $E_h/E_{pl}$  is a measure of the size of the hump with respect to the power law. The bottom left panel of Fig. 14 shows the  $\log_{10}$  of this ratio as a function of  $\log_{10}(T_p/T_h)$ . The horizontal dotted line indicates the ratio value for which there is no excess late hump over and above the power law decay. A simple explanation for the observed correlation is that the weak hump component is always present at a flux level a factor of  $\sim 10^4$  below the prompt emission and lasts for  $\sim 1000 \times T_p$  seconds, but it is only detected if the initial decay is fast with  $\alpha_0\alpha_d > 1.9$ . If the decay from the prompt phase is slow then, by the time the flux has dropped to the appropriate level, the hump component has faded away.

The bottom right-hand panel of Fig. 14 shows the  $\log_{10}$  of the fluence ratio  $E_h/E_{pl}$  plotted vs.  $\alpha_f$ . There is a significant correlation (coefficient 0.60, significant at  $> 99.9\%$ ) between the two indicating that the late hump is more visible when the decay conforms to the high latitude model ( $\alpha_f \geq 2$ ) but becomes obscured if an afterglow component dominates.

We can also integrate the light curves for  $t < T_p$  to find the fluence of the prompt emission,  $E_{pr}$ . The ratio  $(E_h - E_{pl})/E_{pr}$  is then a measure of the fluence in the excess late hump relative to the prompt fluence. The upper panels of Fig. 14 show  $\log_{10}$  of this ratio with respect to  $\log_{10}(T_p/T_h)$  and  $\alpha_f$ . There is no correlation between the fluence in the excess late hump and temporal decay index or the dominance of the high latitude emission over the afterglow. The GRBs with the largest  $\alpha_f$  values (weak or no afterglow component present) have the highest  $\Delta_H$  and  $E_h/E_{pl}$  values but not the maximum  $(E_h - E_{pl})/E_{pr}$ . The fluence in the late hump is not correlated with the presence of afterglow nor is it correlated with the prompt fluence.

The horizontal dotted line in the top panels of Fig. 14 indicates the level at which the late hump fluence is equal to the prompt fluence. It is interesting that the maximum late hump fluence is commensurate with the prompt fluence, suggestive of some kind of equipartition in energy between these emission phases. Previous analyses of the hump have proposed that it is not consistent with an afterglow component, but is consistent with refreshing of the forward shock either by continued activity from the central engine or a range in initial Lorentz factor of the ejecta (Nousek et al. 2006; Zhang et al. 2006). At the end of energy injection (i.e. the end of the hump) there will be a break in the decay index, the magnitude of which depends on the injection mechanism (Nousek et al. 2006). After this period the

emission is presumably dominated by the afterglow again. Another change in decay index will occur at the jet break. The longest duration humps last almost a day, similar to the timescale on which some jet breaks have been seen (Frail et al. 2001). This raises the possibility that some light curve breaks described as a jet break may be due to the end of energy injection.

The X-ray flares may also be due to the central engine, particularly where the flare fluence is high (e.g. King et al. 2005). In only two cases — GRB050502B and GRB050820A — is there a clear indication that the large, late flare appears to have caused an offset in the later decay (i.e. the flux decays after the flare but does not rejoin the previous decay). We note that Falcone et al. (2006) reach a different conclusion for GRB050502B using XRT data alone. GRB050820A is discussed in detail in Osborne et al. (2006).

The analysis described above has considered just the soft X-ray band, 0.3–10 keV (i.e. the XRT bandpass). We expect the prompt emission to dominate in the hard (BAT) band, 15–150 keV, while the afterglow is predominantly soft X-ray. Fig. 15 shows the ratio of the hard (15–150 keV) fluence for  $t < T_p$ ,  $E_\gamma$ , with the soft (0.3–10 keV) decay fluence for  $t > T_p$ ,  $R_E = E_\gamma / (E_X - E_{pr})$ , where  $E_X$  is the total soft fluence and  $E_{pr}$  is the prompt fluence as before. For GRBs with  $\alpha_f > 1.75$ ,  $R_E = 2.36 \pm 0.93$  while for  $\alpha_f < 0.25$   $R_E = 0.22 \pm 0.13$ . Thus, GRBs with smaller  $\alpha_f$  have a greater fraction of their energy emitted at  $t > T_p$ .

For the GRBs with a known redshift we can use the burst duration,  $T_p$ , to estimate the isotropic equivalent gamma-ray energy,  $E_p$  (1–300) keV, released in the rest-frame 1–300 keV band during the prompt phase,  $t < T_p$ . We have used a rest-frame band similar to that of the BAT to avoid having to extrapolate over a large energy range with a resultant more uncertain k-correction. We assume a cosmology with  $H_0 = 71 \text{ km s}^{-1} \text{ Mpc}^{-1}$ ,  $\Lambda = 0.27$  and  $\Omega = 0.73$ . These energy estimates are shown in the left-hand panel of Fig. 16, plotted against the log of the rest-frame duration of the burst,  $\log_{10}(T_p/(1+z))$ . Most bursts cluster in the center with similar durations and luminosities. GRB050724 and GRB050803 lie towards the bottom right. GRB050724 is a short burst with a long soft X-ray tail (Barthelmy et al. 2005b) which causes a large  $T_p$ . It has a lower luminosity relative to its duration than the long bursts plotted in Fig. 16. A low luminosity for GRB050724 is consistent with other short bursts (Fox et al. 2005). GRB050803 has an uncertain redshift as no clear optical transient was found. The redshift used here ( $z = 0.422$ ) is that of a star-forming galaxy in the XRT error box (Bloom et al. 2005). Either the redshift is under-estimated or this is also an under-luminous burst.

The derived luminosity clearly depends on both the duration and the bandpass over which the original fluence (to be converted into luminosity) is obtained. To illustrate this, we also show in Fig. 16 the isotropic equivalent gamma-ray energy,  $E_{iso}$  (1–300) keV, released

in the rest-frame 1–300 keV band during  $T_{90}$ .

## 9. Conclusions

We have analysed data for the 40 GRBs observed by *Swift* prior to 2005 October 1 for which XRT observations began within 10 minutes of the BAT trigger. We have combined data from the BAT and the XRT to investigate the form of the X-ray emission (0.3–10 keV) during the first few hours following the burst.

The initial XRT spectral index is slightly steeper than that seen in the BAT, showing that spectral evolution occurs as the GRB ages. Combining the BAT and XRT data, the raw light curves show that the initial X-ray emission seen in the XRT is consistent with being a continuation of the emission seen by the BAT. Some two-thirds of the GRBs display a light curve which shows a steeply declining component that breaks to a shallower decay rate – the late emission hump – usually within an hour of the trigger. The remaining bursts decline fairly continuously. At least half of the GRBs in the sample display late X-ray flares, probably due to continued central engine activity, but in only a few GRBs does the fluence in the flares rival that of the burst.

To investigate the early X-ray emission, we used an automatic fitting procedure to align the light curves. Allowing for flares, this procedure works well for the entire sample. The resultant light curves display a prompt phase, mostly observed by the BAT, followed by a decline. The light curve can be described by an exponential which relaxes into a power law whose decay rate varies considerably from burst to burst. The transition time between the exponential and power law provides a well determined measure of the burst duration.

Comparing the temporal and spectral indices of the power law decline, the distribution is consistent with a simple model in which the early emission is a combination of emission from the central engine (parameterised by high latitude emission; Kumar & Panaitescu (2000)) and afterglow. Those GRBs in which the afterglow is weak early on decay fast during the power law phase and their X-ray light curves are consistent with the high latitude model. Some are dominated by afterglow, while the majority require a significant contribution from both components. The likelihood of an early optical detection strongly correlates with the strength of the X-ray afterglow component.

The late emission hump component may be present in all objects but can be masked by a strong afterglow component. The late hump can last for many tens of thousands of seconds and may also be due to continued central engine activity (Nousek et al. 2006; Zhang et al. 2006). Interestingly, the strongest humps seen have a total fluence which matches that of

the prompt phase. There appears to be a correlation such that bursts with the most visible humps do not have strong, late X-ray flares.

**Acknowledgments** MRG, JPO, KP, APB, SV, ER and OG gratefully acknowledge funding through the PPARC. This work is also supported at Pennsylvania State University (PSU) by NASA contract NAS5-00136 and NASA grant NNG05GF43G, and at the Osservatorio Astronomico di Brera (OAB) by funding from ASI on grant number I/R/039/04. We gratefully acknowledge the contributions of numerous colleagues at Leicester University, PSU, OAB, Goddard Space Flight Center and our sub-contractors, who helped make the BAT and XRT possible.

## REFERENCES

- Anders, E., Ebihara, M., 1982, *Geochimica et Cosmochimica Acta*, 46, 2363
- Arnaud, K., 1996, in Jacoby G., Barnes J., eds, *Astronomical Data Analysis Software and systems*, ASP Conf. Series Vol 101, p17
- Band, D.L., 2006, *ApJ*, submitted (astro-ph/0602267)
- Barthelmy, S.D. et al., 2005a, *Sp. Sc. Rev.*, 120, 143
- Barthelmy, S.D. et al., 2005b, *Nature*, 438, 994
- Beardmore, A.P. et al., 2006, *MNRAS*, submitted
- Berger, E. et al., 2005, *ApJ*, 634, 501
- Berger, E. Cenko, S.B., Kukarni, S.R., 2005, *GCN* 3088
- Bloom, J.S., Perley, D., Foley, R., Prochaska, J.X., Chen, H.-W., & Starr, D., 2005, *GCN* 3758
- Bloom, J.S. et al., 2006, *ApJ*, 638, 354
- Blustin, A. et al, 2006, *ApJ*, 637, 901
- Burrows, D.N. et al., 2005a, *Science*, 309, 1833
- Burrows, D.N. et al., 2005b, *Sp. Sc. Rev.*, 120, 165
- Burrows, D.N. et al., 2005c, *ApJ*, 622, L85

- Burrows, D.N. et al., 2006, ApJ, submitted (astro-ph/0604320)
- Campana, S. et al., 2005, ApJ, 625, L23
- Campana, S. et al., 2006, A&A, in press
- Cenko, S.B., Kulkarni, S.R., Gal-Yam, A., & Berger, E., 2005, GCN 3542
- Chen, H.-W., Thompson, I., Prochaska, J.X., & Bloom, J., 2005, GCN 3709
- Cusumano, G. et al., 2006, ApJ, 639, 316
- Dickey, J.M., & Lockman F.J., 1990, ARA&A, 28, 215
- Dykes, J., Zhang, B., Fan, Y.Z., 2006, ApJ, submitted (astro-ph/0511699)
- Falcone, A. et. al., 2006, ApJ, 641, 1010
- Fishman, G.J. et al. 1994, ApJS, 92, 229
- Foley, R.J., Chen, H.-W., & Bloom, J., 2005, GCN 3483
- Frail, D.A. et al. 2001, ApJ, 562, L55
- Ford, L.H. et al., 1995, ApJ, 439, 307
- Fox, D.B. et al., 2005, Nature, 437, 845
- Fugazza, D. et al., 2005, GCN 3948
- Fynbo, J.P.U. et al., 2005a, GCN 3136
- Fynbo, J.P.U. et al., 2005b, GCN 3176
- Fynbo, J.P.U. et al., 2005c, GCN 3749
- Gehrels, N. et al., 2004, ApJ, 611, 1005
- Gehrels, N. et al., 2005, Nature, 437, 851
- Goad, M.R. et al., 2006, A&A, 449, 89
- Godet, O. et al., 2006, A&A, 452, 819
- Granot, J., & Kumar, P., 2006, MNRAS, 366, L13
- Hill, J.E. et al., 2004, SPIE, 5165, 217

- Hill, J.E. et al., 2006, *ApJ*, 639, 303
- Hjorth, J. et al., 2005, *Nature*, 437, 859
- Jakobsson, P. et al., 2005, *GCN* 4029
- Kawai, N., Yamada, T., Kosugi, G., Hattori, T., & Aoki, K., 2005, *GCN* 3937
- Kelson, D., & Berger, E., 2005, *GCN* 3101
- King, A., O’Brien, P.T., Goad, M.R., Osborne, J., Olsson, E., & Page, K., 2005, *ApJ*, 630, L113
- Kouveliotou, C. et al., 1993, *ApJ*, 413, L101
- Krimm, H., Parsons, A., & Markwardt, C., 2004, “BAT Ground Analysis Software Manual” (<http://heasarc.gsfc.nasa.gov/docs/swift/analysis>)
- Kumar, P., Panaitescu, A., 2000, *ApJ*, 541, L51
- Levan, A. et al., 2006, *ApJ*, submitted (astro-ph/0605256)
- MacFadyen, A.L., & Woosley, S.E., 1999, *ApJ*, 524, 262
- Mészáros, P. & Rees, M.J., 1997, *ApJ*, 476, 232
- Mészáros, P. & Rees, M.J., 2000, *ApJ*, 530, 292
- Mészáros, P. & Rees, M.J., 2001, *ApJ*, 556, L37
- Morrison, R., McCammon, D., 1983, *ApJ*, 270, 119
- Nousek, J.A. et al. 2006, *ApJ*, 642, 389
- Osborne, J. et al. 2006, in prep
- Paczyński B., 1998, *ApJ*, 494, L45
- Panaitescu, A. & Kumar, P., 2002, *ApJ*, 571, 779
- Panaitescu, A., Mészáros, P., Gehrels, N., Burrows, D., & Nousek, J., 2006, *MNRAS*, 366, 1357
- Prochaska, J.X., Chen, H.-W., Bloom, J., & Stevens, A., 2005a, *GCN* 3679
- Prochaska, J.X. et al., 2005b, *GCN* 3833

- Rees, M.J. & Mészáros, P. 1994, ApJ, 430, L93
- Rees, M.J. & Mészáros, P., 1998, ApJ, 496, L1
- Reichart, D.E. & Price, P.A., 2002, ApJ, 565, 174
- Roming, P.W.A. et al., 2005, Sp. Sc. Rev., 120, 95
- Sari, R., & Mészáros, P., 2000, ApJ, 535, L33
- Sari, R., & Piran, T. 1997, ApJ, 485, 270
- Sari, R., Piran, T. & Narayan, R., 1998, ApJ, 497, L17
- Tagliaferri, G. et al., 2005, Nature, 436, 985
- Vaughan, S. et al., 2006a, ApJ, 638, 920
- Vaughan, S. et al., 2006b, ApJ, 639, 323
- Yost, S., Harrison, F.A., Sari, R., & Frail, D.A., 2003, ApJ, 597, 459
- Zhang, B et al., 2006, ApJ, 642, 354
- Zhang, B. & Mészáros, P., 2001, ApJ, 566, 712
- Zhang, B. & Mészáros, P., 2002, ApJ, 571, 876

Table 1. GRB sample and BAT data

GRB	T <sub>90</sub>	T <sub>50</sub>	$\beta_b$	BAT mean flux (15–150 keV) (10 <sup>−8</sup> erg cm <sup>−2</sup> s <sup>−1</sup> )	Redshift	Ref. <sup>†</sup>
	(s)	(s)				
050126	25.7 ± 0.3	13.7 ± 0.3	0.41 ± 0.15	3.15 ± 0.28	1.29	1
050128	28.0 ± 0.2	8.0 ± 0.2	0.41 ± 0.08	17.1 ± 0.71		
050219A	23.5 ± 0.3	9.9 ± 0.2	0.35 ± 0.05	16.7 ± 0.51		
050315	96.0 ± 0.5	24.7 ± 0.4	1.15 ± 0.09	3.23 ± 0.14	1.949	2
050319	149.6 ± 0.7	58 ± 0.5	1.10 ± 0.20	0.54 ± 0.05	3.24	3
050401	33.3 ± 2.0	25.8 ± 1.0	0.52 ± 0.07	22.3 ± 0.88	2.90	4
050406	5.7 ± 0.2	2.4 ± 0.3	1.64 ± 0.47	1.35 ± 0.31		
050412	24.1 ± 2.0	8.4 ± 1.0	−0.26 ± 0.18	2.22 ± 0.22		
050416A	2.4 ± 0.3	0.7 ± 0.2	2.20 ± 0.25	13.76 ± 1.31	0.6535	5
050421	10.3 ± 0.2	5.1 ± 0.2	0.64 ± 0.46	1.04 ± 0.29		
050422	59.2 ± 0.3	42.8 ± 0.3	0.54 ± 0.21	0.97 ± 0.12		
050502B	17.5 ± 0.2	9.8 ± 0.2	0.64 ± 0.15	2.57 ± 0.23		
050525A	8.8 ± 0.5	5.2 ± 0.4	0.83 ± 0.02	175.9 ± 2.32	0.606	6
050607	26.5 ± 0.2	13.7 ± 0.2	0.97 ± 0.17	2.15 ± 0.20		
050712	48.4 ± 2.0	25.6 ± 1.0	0.50 ± 0.19	1.96 ± 0.22		
050713A	128.8 ± 10	11.4 ± 10	0.55 ± 0.07	3.81 ± 0.14		
050713B	131.0 ± 3.0	44.0 ± 0.7	0.53 ± 0.15	3.21 ± 0.27		
050714B	46.4 ± 0.4	21.4 ± 0.3	1.70 ± 0.41	1.13 ± 0.21		
050716	69.4 ± 1.0	36.0 ± 0.5	0.47 ± 0.06	8.76 ± 0.30		
050717	67.2 ± 2.0	24.8 ± 1.0	0.36 ± 0.05	8.63 ± 0.20		
050721	39.2 ± 0.5	15.0 ± 0.5	0.78 ± 0.12	7.11 ± 0.48		
050724*	152.5 ± 9.0	84.6 ± 3.0	1.17 ± 0.26	0.74 ± 0.09	0.257	7
050726	33.9 ± 0.2	15.0 ± 0.5	0.01 ± 0.17	4.84 ± 0.43		
050730	155.0 ± 2.1	63.0 ± 1.6	0.52 ± 0.11	1.48 ± 0.09	3.97	8
050801	20.0 ± 3.0	6.0 ± 1.0	1.03 ± 0.24	1.52 ± 0.22		
050802	30.9 ± 1.0	9.3 ± 0.5	0.66 ± 0.15	6.08 ± 0.52	1.71	9
050803	89.0 ± 10	40.0 ± 5.0	0.47 ± 0.11	2.38 ± 0.15	(0.422) <sup>‡</sup>	10
050813*	0.58 ± 0.1	0.26 ± 0.1	0.37 ± 0.37	8.52 ± 0.20		
050814	144.0 ± 3.0	56.0 ± 1.2	0.98 ± 0.19	1.22 ± 0.13		



Table 1—Continued

GRB	T <sub>90</sub>	T <sub>50</sub>	$\beta_b$	BAT mean flux (15–150 keV) ( $10^{-8}$ erg cm <sup>-2</sup> s <sup>-1</sup> )	Redshift	Ref. <sup>†</sup>
	(s)	(s)				
050819	35.8 ± 4.0	16.4 ± 1.0	1.56 ± 0.21	0.91 ± 0.14		
050820A	240 ± 5.0	221 ± 5.0	0.24 ± 0.07	1.57 ± 0.11	2.612	11
050822	105 ± 2.0	43.8 ± 1.0	1.53 ± 0.09	2.54 ± 0.16		
050826	35.3 ± 8.0	14.8 ± 2.0	0.10 ± 0.28	1.18 ± 0.19		
050904	173.2 ± 10	53.3 ± 5.0	0.38 ± 0.04	2.74 ± 0.10	6.29	12
050908	20.3 ± 2.0	6.7 ± 1.0	0.91 ± 0.11	2.41 ± 0.26	3.35	13
050915A	41.8 ± 3.0	14.2 ± 1.0	0.37 ± 0.11	1.79 ± 0.18		
050915B	39.5 ± 1.0	21.3 ± 0.6	0.89 ± 0.06	8.61 ± 0.34		
050916	92.1 ± 10	32.0 ± 4.0	0.83 ± 0.32	1.19 ± 0.16		
050922B	150 ± 15	25.0 ± 5.0	1.11 ± 0.16	1.25 ± 0.18		
050922C	4.1 ± 1.0	1.4 ± 0.5	0.34 ± 0.03	35.7 ± 1.05	2.198	14

\*Would have appeared as a short burst to BATSE.

‡Uncertain identification. Redshift given is that of a star-forming galaxy in XRT error box.

†Redshift references. 1: Berger, Cenko, & Kulkarni (2005). 2: Kelson & Berger (2005). 3: Fynbo et al. (2005a). 4: Fynbo et al. (2005b). 5: Cenko et al. (2005). 6: Foley, Chen & Bloom (2005). 7: Prochaska et al. (2005a). 8: Chen et al. (2005). 9: Fynbo et al. (2005c). 10: Bloom et al. (2005). 11: Prochaska et al. (2005b). 12: Kawai et al. (2005). 13: Fugazza et al. (2005). 14: Jakobsson et al. (2005).

Table 2. BAT fits for those bursts better-fitted with a cutoff power law

GRB	BAT $\beta_{bc}$	$E_{\text{cut}}$ keV	$\Delta\chi^2{}^\dagger$
050128	$-0.53^{+0.35}_{-0.37}$	$65.4^{+39.6}_{-18.6}$	23.8
050219A	$-1.03^{+0.28}_{-0.30}$	$43.2^{+10.8}_{-7.60}$	88.3
050525A	$-0.17^{+0.12}_{-0.12}$	$63.8^{+8.30}_{-6.70}$	246.6
050716	$-0.17^{+0.27}_{-0.29}$	$89.1^{+61.6}_{-27.4}$	18.0

<sup>†</sup>Improvement in  $\chi^2$  for one degree of freedom.

Table 3. XRT spectral and temporal fits

GRB	XRT start (s)	XRT $\beta_x$	Galactic $N_H$ ( $10^{20} \text{ cm}^{-2}$ )	Intrinsic	$\alpha_1$	$t_{\text{break}}$ (s)	$\alpha_2$
050126	127	$1.59 \pm 0.38$	5.30		$2.52^{+0.50}_{-0.22}$	$424^{+561}_{-120}$	$1.00^{+0.17}_{-0.26}$
050128	227	$0.85 \pm 0.12$	4.80	$7.67^{+2.06}_{-1.85}$	$0.66^{+0.10}_{-0.11}$	$1724^{+937}_{-565}$	$1.16^{+0.09}_{-0.08}$
050219A	92	$1.02 \pm 0.20$	8.50	$17.0^{+7.00}_{-6.40}$	$3.17^{+0.24}_{-0.16}$	$332^{+26}_{-22}$	$0.75^{+0.09}_{-0.07}$
050315	83	$1.50 \pm 0.40$	4.30	$122^{+46.0*}_{-38.0}$	$5.30^{+0.50}_{-0.40}$	$400^{+20}_{-20}$	$0.71^{+0.04}_{-0.04}$
050319	211	$2.02 \pm 0.47$	1.10		$3.80^{+0.56}_{-0.56}$	$424^{+38}_{-35}$	$0.47^{+0.10}_{-0.10}$
050401	128	$0.98 \pm 0.05$	4.80	$170^{+37.0*}_{-34.0}$	$0.76^{+0.02}_{-0.02}$	$5518^{+1149}_{-1043}$	$1.31^{+0.05}_{-0.05}$
050406	84	$1.37 \pm 0.25$	3.00		$1.05^{+0.57}_{-0.51}$		
050412	99	$0.26 \pm 0.32$	2.20		$1.81^{+0.57}_{-0.47}$		
050416A	87	$0.80 \pm 0.29$	2.10	$46.8^{+31.7*}_{-25.2}$	$0.87^{+0.45}_{-0.45}$	$400^{+221}_{-264}$	$0.24^{+0.44}_{-0.24}$
050421	110	$0.27 \pm 0.37$	14.4	$61.0^{+42.0}_{-35.0}$	$3.05^{+0.17}_{-0.15}$		
050422	109	$2.33 \pm 0.60$	100		$5.31^{+0.66}_{-0.60}$	$341^{+154}_{-72}$	$0.59^{+0.20}_{-0.27}$
050502B	63	$0.81 \pm 0.28$	3.70		$1.35^{+0.31}_{-0.27}$		
050525A	125	$1.07 \pm 0.02$	9.00	$38.0^{+3.40*}_{-3.00}$	$0.98^{+0.05}_{-0.05}$	$641^{+690}_{-123}$	$1.39^{+0.09}_{-0.04}$
050607	84	$0.77 \pm 0.48$	14.0		$1.94^{+0.17}_{-0.17}$	$1217^{+372}_{-276}$	$0.54^{+0.05}_{-0.05}$
050712	166	$0.90 \pm 0.06$	13.0		$1.34^{+0.10}_{-0.10}$	$3987^{+2576}_{-2064}$	$0.76^{+0.10}_{-0.10}$
050713A	73	$1.30 \pm 0.07$	11.0	$42.0^{+3.20}_{-2.90}$	$2.29^{+0.13}_{-0.14}$	$321^{+107}_{-38}$	$0.71^{+0.08}_{-0.17}$
050713B	136	$0.70 \pm 0.11$	18.0	$20.0^{+4.90}_{-4.50}$	$2.88^{+0.14}_{-0.13}$	$540^{+47}_{-44}$	$0.43^{+0.06}_{-0.06}$
050714B	151	$4.50 \pm 0.70$	5.30	$63.0^{+13.4}_{-11.7}$	$6.96^{+0.60}_{-0.60}$	$366^{+38}_{-38}$	$0.52^{+0.11}_{-0.11}$
050716	96	$0.33 \pm 0.03$	11.0		$2.09^{+0.04}_{-0.03}$	$1700^{+434}_{-329}$	$1.02^{+0.07}_{-0.08}$
050717	79	$0.63 \pm 0.11$	23.0	$31.0^{+6.50}_{-6.10}$	$1.95^{+0.18}_{-0.11}$	$318^{+115}_{-95}$	$1.29^{+0.08}_{-0.08}$
050721	186	$0.74 \pm 0.15$	16.0	$19.0^{+6.40}_{-5.70}$	$2.35^{+0.16}_{-0.16}$	$380^{+30}_{-30}$	$1.22^{+0.03}_{-0.03}$
050724	74	$0.95 \pm 0.07$	$59^\dagger$		$4.03^{+0.18}_{-0.15}$	$508^{+120}_{-31}$	$1.82^{+0.24}_{-0.28}$
050726	110	$0.94 \pm 0.07$	4.70		$0.97^{+0.30}_{-0.30}$	$7754^{+1646}_{-2162}$	$1.78^{+0.30}_{-0.25}$
050730	130	$0.33 \pm 0.08$	3.10	$140^{+37.0*}_{-35.0}$	$2.21^{+0.44}_{-0.44}$	$222^{+25}_{-21}$	$0.35^{+0.30}_{-0.20}$
050801	61	$0.72 \pm 0.54$	7.00		$0.96^{+0.04}_{-0.04}$		
050802	289	$0.91 \pm 0.19$	1.80		$0.64^{+0.10}_{-0.09}$	$6036^{+1667}_{-850}$	$1.66^{+0.06}_{-0.06}$
050803	152	$0.71 \pm 0.16$	5.60	$20.0^{+8.60*}_{-7.70}$	$5.15^{+0.26}_{-0.26}$	$272^{+12}_{-8}$	$0.59^{+0.03}_{-0.04}$
050813	73	$2.42 \pm 0.89$	4.00		$2.00^{+0.61}_{-0.50}$		
050814	138	$1.08 \pm 0.08$	2.60	$2.20^{+1.35}_{-1.27}$	$3.03^{+0.09}_{-0.08}$	$1039^{+130}_{-109}$	$0.66^{+0.08}_{-0.08}$
050819	141	$1.18 \pm 0.23$	4.70		$4.39^{+0.50}_{-0.50}$	$269^{+40}_{-21}$	$2.09^{+0.53}_{-0.57}$

Table 3—Continued

GRB	XRT start (s)	XRT $\beta_x$	Galactic $N_H$ ( $10^{20}$ cm $^{-2}$ )	Intrinsic	$\alpha_1$	$t_{\text{break}}$ (s)	$\alpha_2$
050820A	80	$0.87 \pm 0.09$	4.60		$2.22^{+0.23}_{-0.22}$	$2060^{+1850}_{-1850}$	$1.13^{+0.02}_{-0.02}$
050822	96	$1.60 \pm 0.06$	2.30	$13.0^{+1.00}_{-0.90}$	$2.81^{+0.25}_{-0.25}$	$279^{+117}_{-117}$	$0.39^{+0.12}_{-0.14}$
050826	109	$1.27 \pm 0.47$	22.0	$65.0^{+51.8}_{-44.2}$	$1.19^{+0.07}_{-0.05}$		
050904	161	$0.44 \pm 0.04$	4.90	$355^{+10.0*}_{-97.0}$	$1.81^{+0.06}_{-0.06}$		
050908	106	$2.35 \pm 0.27$	2.10		$1.04^{+0.07}_{-0.13}$		
050915A	87	$1.12 \pm 0.34$	1.90	$15.0^{+9.00}_{-9.00}$	$2.87^{+1.40}_{-1.40}$	$144^{+21}_{-30}$	$0.89^{+0.03}_{-0.03}$
050915B	136	$1.45 \pm 0.10$	30.0		$5.21^{+0.16}_{-0.16}$	$437^{+15}_{-15}$	$0.66^{+0.08}_{-0.08}$
050916	210	$0.77 \pm 0.84$	122		$0.79^{+0.08}_{-0.08}$		
050922B	342	$1.64 \pm 0.08$	3.40	$12.0^{+1.70}_{-1.50}$	$3.04^{+0.18}_{-0.18}$	$2971^{+388}_{-388}$	$0.30^{+0.08}_{-0.08}$
050922C	108	$1.10 \pm 0.09$	5.80		$1.19^{+0.02}_{-0.02}$		

\*In rest-frame.

<sup>†</sup>Vaughan et al. (2006b)

Table 4. Best fit parameters derived from the average X-ray decay curve.

GRB	$\alpha_0\alpha_d$	$\Delta_F$	$\Delta_H$	$T_p$	$\alpha_f$
050126	$2.36 \pm 0.20$	$-0.03 \pm 0.31$	$2.15 \pm 0.31$	$35.1 \pm 2.9$	$1.14 \pm 0.49$
050128	$1.13 \pm 0.16$	$0.01 \pm 0.12$		$38.7 \pm 5.3$	$0.93 \pm 0.34$
050219A	$1.55 \pm 0.32$	$0.03 \pm 0.22$	$1.06 \pm 0.31$	$39.8 \pm 8.2$	$1.56 \pm 0.42$
050315	$4.17 \pm 0.56$	$0.08 \pm 0.28$	$9.72 \pm 0.18$	$64.2 \pm 8.7$	$3.27 \pm 0.99$
050319	$2.49 \pm 0.51$	$0.40 \pm 0.22$	$3.00 \pm 0.23$	$35.3 \pm 7.2$	$0.25 \pm 1.04$
050401	$1.17 \pm 0.19$	$0.08 \pm 0.15$	$0.01 \pm 0.89$	$16.6 \pm 2.6$	$0.06 \pm 0.24$
050406	$1.96 \pm 0.44$	$0.48 \pm 0.32$	$0.73 \pm 0.47$	$7.3 \pm 1.6$	$-0.47 \pm 0.95$
050412	$0.90 \pm 0.14$	$0.10 \pm 0.28$		$12.7 \pm 1.9$	$0.90 \pm 0.31$
050416A	$2.00 \pm 0.78$	$-0.32 \pm 0.61$	$2.29 \pm 0.23$	$7.7 \pm 3.0$	$-0.40 \pm 1.33$
050421	$2.95 \pm 0.22$	$0.03 \pm 0.38$		$172 \pm 13$	$2.56 \pm 0.60$
050422	$3.84 \pm 0.35$	$0.00 \pm 0.23$	$7.22 \pm 0.29$	$46.5 \pm 4.2$	$2.70 \pm 1.49$
050502B	$2.23 \pm 0.53$	$2.08 \pm 0.40$	$3.92 \pm 0.23$	$32.5 \pm 7.8$	$1.39 \pm 0.71$
050525A	$1.40 \pm 0.33$	$0.29 \pm 0.24$	$0.51 \pm 0.23$	$9.0 \pm 2.1$	$0.82 \pm 0.38$
050607	$2.00 \pm 0.53$	$0.49 \pm 0.23$	$1.77 \pm 0.21$	$26.6 \pm 7.0$	$0.89 \pm 0.83$
050712	$1.61 \pm 0.28$	$0.04 \pm 0.12$	$1.22 \pm 0.49$	$131 \pm 22$	$0.68 \pm 0.38$
050713A	$2.51 \pm 0.17$	$1.15 \pm 0.12$	$3.98 \pm 0.14$	$13.9 \pm 0.9$	$1.46 \pm 0.24$
050713B	$3.03 \pm 0.24$	$0.03 \pm 0.18$	$5.54 \pm 0.41$	$143 \pm 11$	$2.49 \pm 0.33$
050714B	$2.50 \pm 0.43$	$0.20 \pm 0.19$	$3.09 \pm 0.27$	$96 \pm 17$	$-0.09 \pm 1.06$
050716	$1.64 \pm 0.18$	$0.09 \pm 0.08$	$0.69 \pm 0.30$	$124. \pm 14$	$1.55 \pm 0.29$
050717	$1.73 \pm 0.17$	$0.02 \pm 0.11$	$0.55 \pm 0.71$	$58.4 \pm 5.7$	$1.13 \pm 0.22$
050721	$1.72 \pm 0.15$	$-0.04 \pm 0.12$	$1.02 \pm 0.49$	$56.0 \pm 5.0$	$0.71 \pm 0.26$
050724	$2.66 \pm 0.23$	$0.04 \pm 0.14$	$3.09 \pm 0.30$	$181 \pm 16$	$1.45 \pm 0.43$
050726	$1.36 \pm 0.20$	$0.06 \pm 0.10$		$46.5 \pm 7.0$	$0.73 \pm 0.28$
050730	$0.87 \pm 0.24$	$0.16 \pm 0.12$		$373 \pm 102$	$0.25 \pm 0.29$
050801	$1.32 \pm 0.24$	$-0.02 \pm 0.23$	$0.44 \pm 0.33$	$10.3 \pm 1.9$	$0.01 \pm 0.64$
050802	$1.24 \pm 0.15$	$0.12 \pm 0.10$	$0.29 \pm 0.18$	$11.1 \pm 1.3$	$0.08 \pm 0.29$
050803	$2.21 \pm 0.27$	$0.43 \pm 0.15$	$2.56 \pm 0.15$	$94 \pm 11$	$1.56 \pm 0.36$
050813	$1.73 \pm 0.21$	$0.21 \pm 0.42$	$0.30 \pm 0.38$	$0.7 \pm 0.1$	$-0.56 \pm 1.16$
050814	$2.81 \pm 0.20$	$0.03 \pm 0.10$	$2.55 \pm 0.29$	$131 \pm 9.5$	$1.71 \pm 0.35$
050819	$3.13 \pm 0.43$	$-0.01 \pm 0.27$	$3.69 \pm 0.43$	$55.6 \pm 7.6$	$1.64 \pm 0.75$
050820A	$0.95 \pm 0.24$	$0.66 \pm 0.17$	$0.17 \pm 0.38$	$19.3 \pm 4.8$	$0.14 \pm 0.29$

Table 4—Continued

GRB	$\alpha_0\alpha_d$	$\Delta_F$	$\Delta_H$	$T_p$	$\alpha_f$
050822	$2.24 \pm 0.46$	$0.45 \pm 0.08$	$2.98 \pm 0.29$	$140 \pm 29$	$-0.17 \pm 0.77$
050826	$1.13 \pm 0.17$	$0.17 \pm 0.26$	$0.29 \pm 0.30$	$15.5 \pm 2.3$	$0.13 \pm 0.53$
050904	$1.69 \pm 0.26$	$0.46 \pm 0.13$	$0.59 \pm 0.40$	$460 \pm 71$	$1.20 \pm 0.30$
050908	$2.84 \pm 0.42$	$0.75 \pm 0.28$	$3.29 \pm 0.38$	$42.9 \pm 6.3$	$0.66 \pm 0.80$
050915A	$3.76 \pm 0.45$	$0.31 \pm 0.21$	$6.40 \pm 0.37$	$79.9 \pm 9.5$	$3.24 \pm 0.66$
050915B	$3.33 \pm 0.52$	$-0.01 \pm 0.19$	$3.93 \pm 0.39$	$82 \pm 13$	$2.23 \pm 0.75$
050916	$2.63 \pm 0.41$	$-0.11 \pm 0.54$	$4.06 \pm 0.21$	$84 \pm 13$	$1.79 \pm 1.02$
050922B	$2.34 \pm 0.22$	$0.16 \pm 0.08$	$2.53 \pm 0.29$	$143 \pm 13$	$0.43 \pm 0.39$
050922C	$1.17 \pm 0.17$	$0.03 \pm 0.09$	$-0.18 \pm 0.37$	$19.4 \pm 2.8$	$0.10 \pm 0.23$

Table 5. Summary of significant correlations

Variables*	Spearman Corr. Coeff.	Significance (%)
$\alpha_1, \beta_x$	0.30	95
$(\alpha_1 - \beta_x), \alpha_1$	0.89	$\gg 99.9$
$\alpha_0\alpha_d, \beta$ (entire sample)	0.53	99
$\alpha_0\alpha_d, \beta$ (GRBs below high lat. line in Fig. 13)	0.66	$\gg 99.9$
$E_h/E_{pl}, \alpha_f$	0.60	$> 99.9$

\*Defined in text.

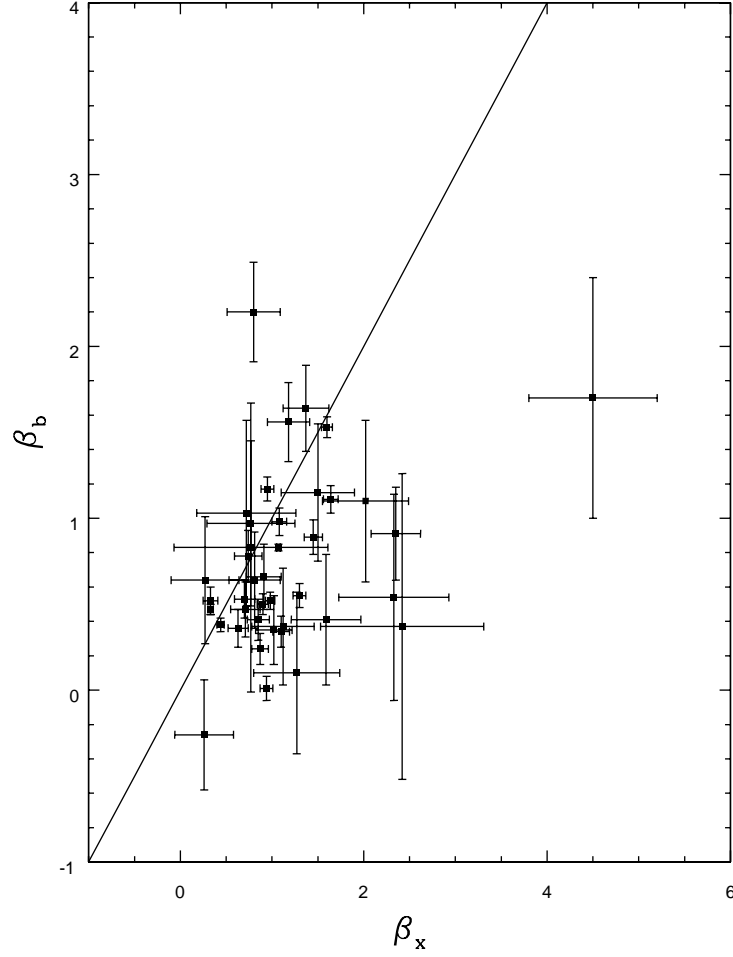


Fig. 1.— The relationship between the BAT ( $\beta_b$ ) and early XRT ( $\beta_x$ ) spectral indices. The solid line shows equality. This plot illustrates that the early X-ray spectrum observed by the XRT tends to be softer than the prompt gamma-ray emission observed by the BAT.



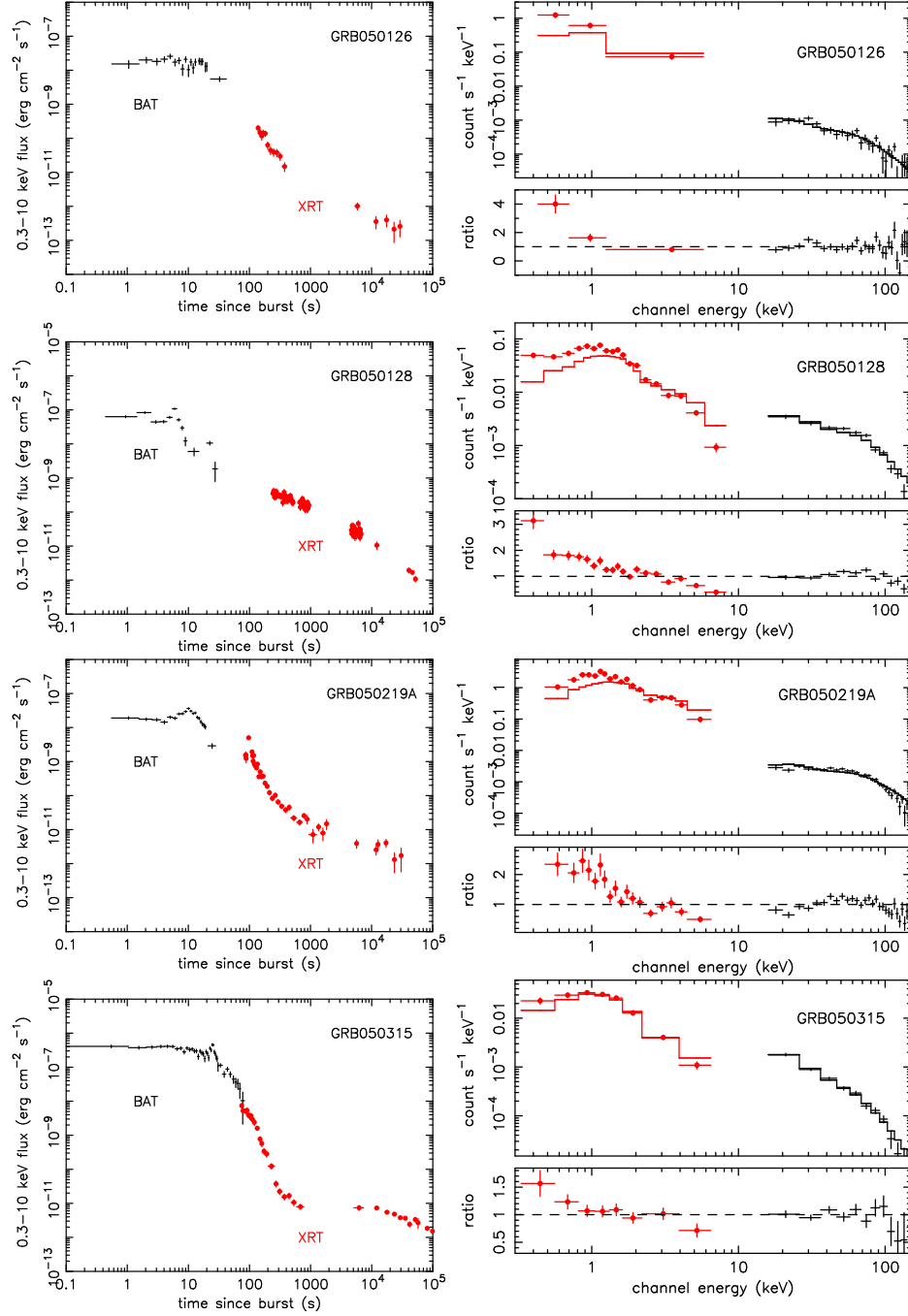


Fig. 2.— Left-hand panels show the combined BAT+XRT unabsorbed 0.3–10 keV flux light curves plotted out to  $10^5$ s. Right-hand panels show the spectra relative to the power law derived from fitting the BAT data. These plots were constructed as described in the text.

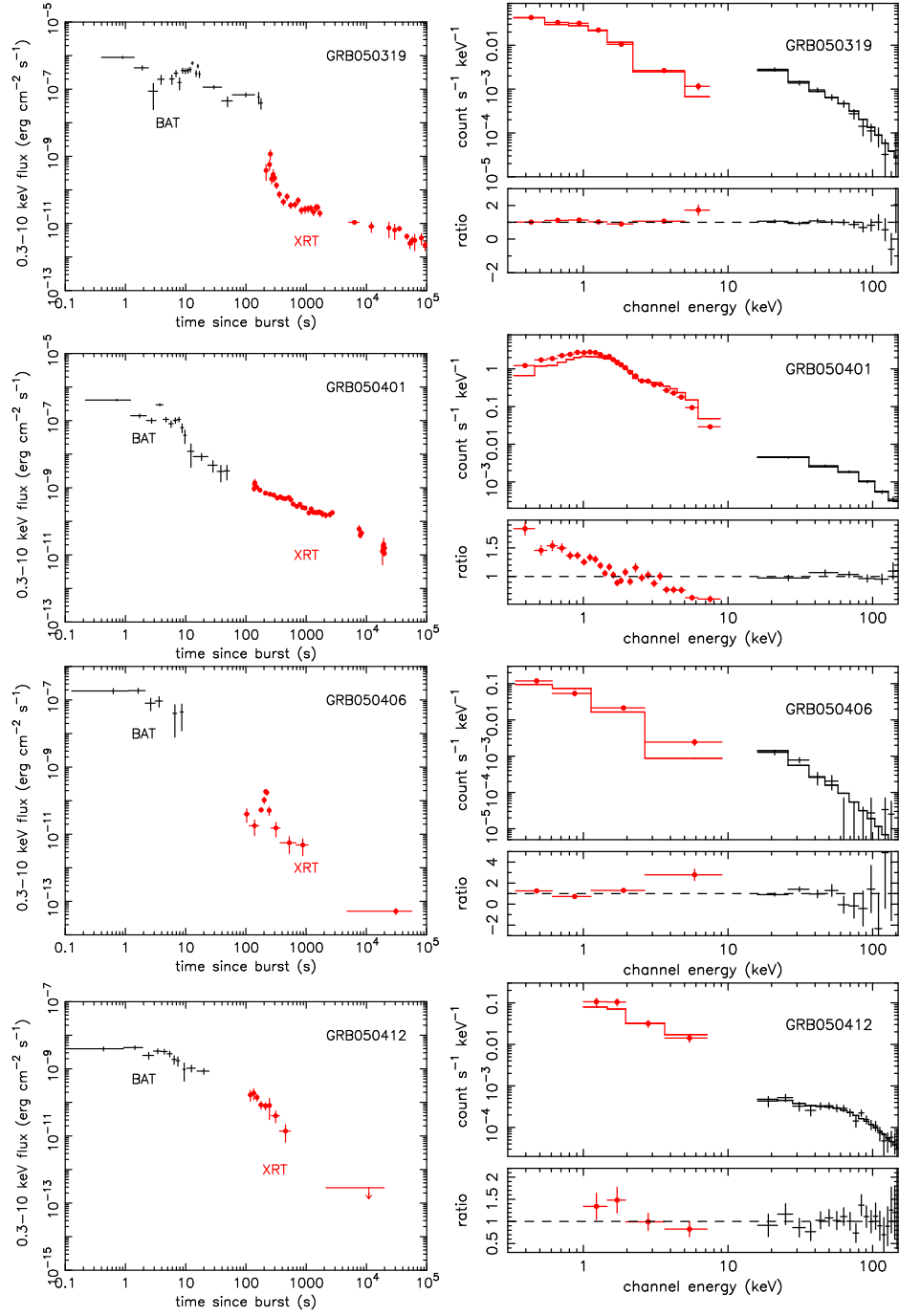


Fig. 2. — continued.

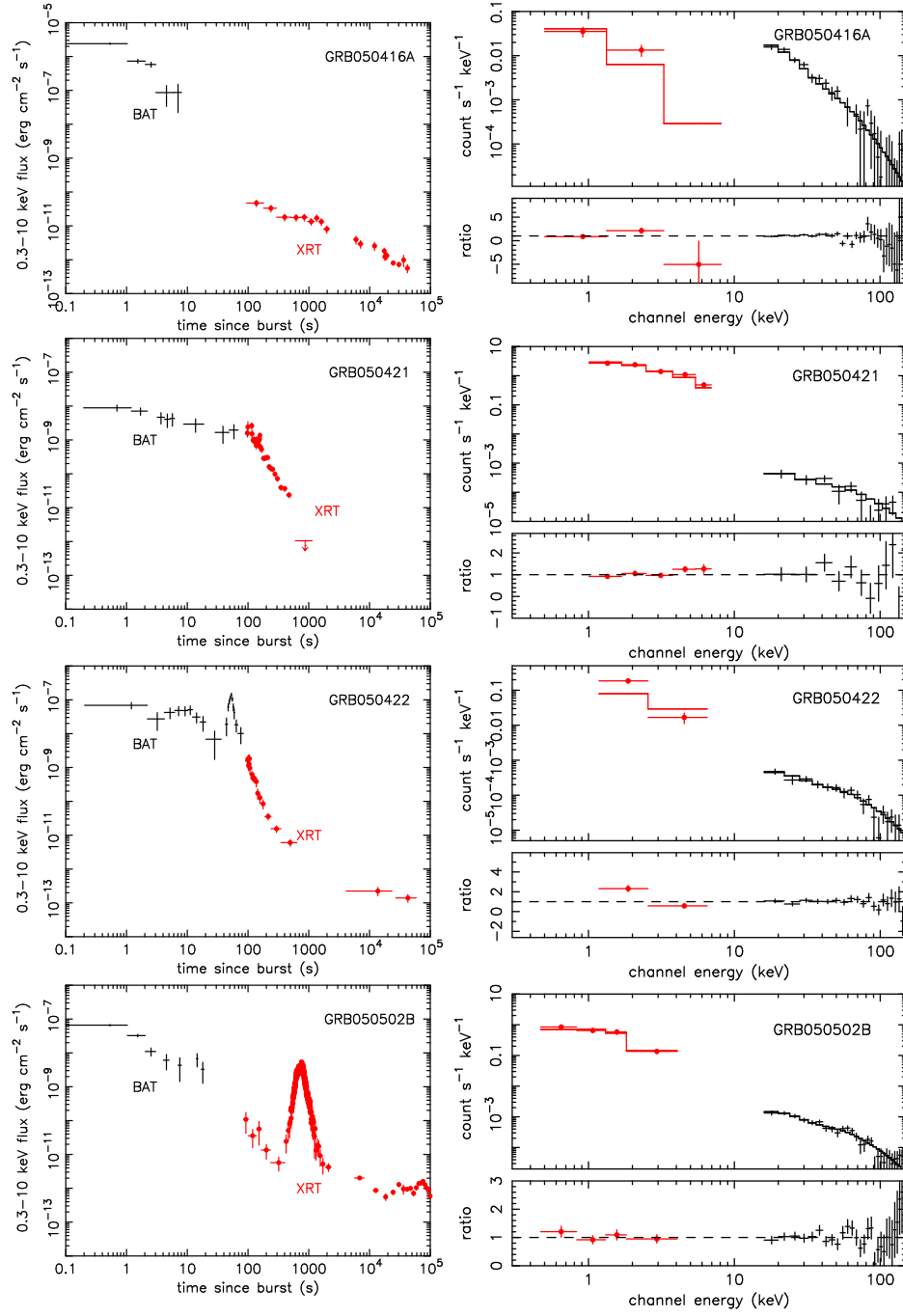


Fig. 2. — continued.

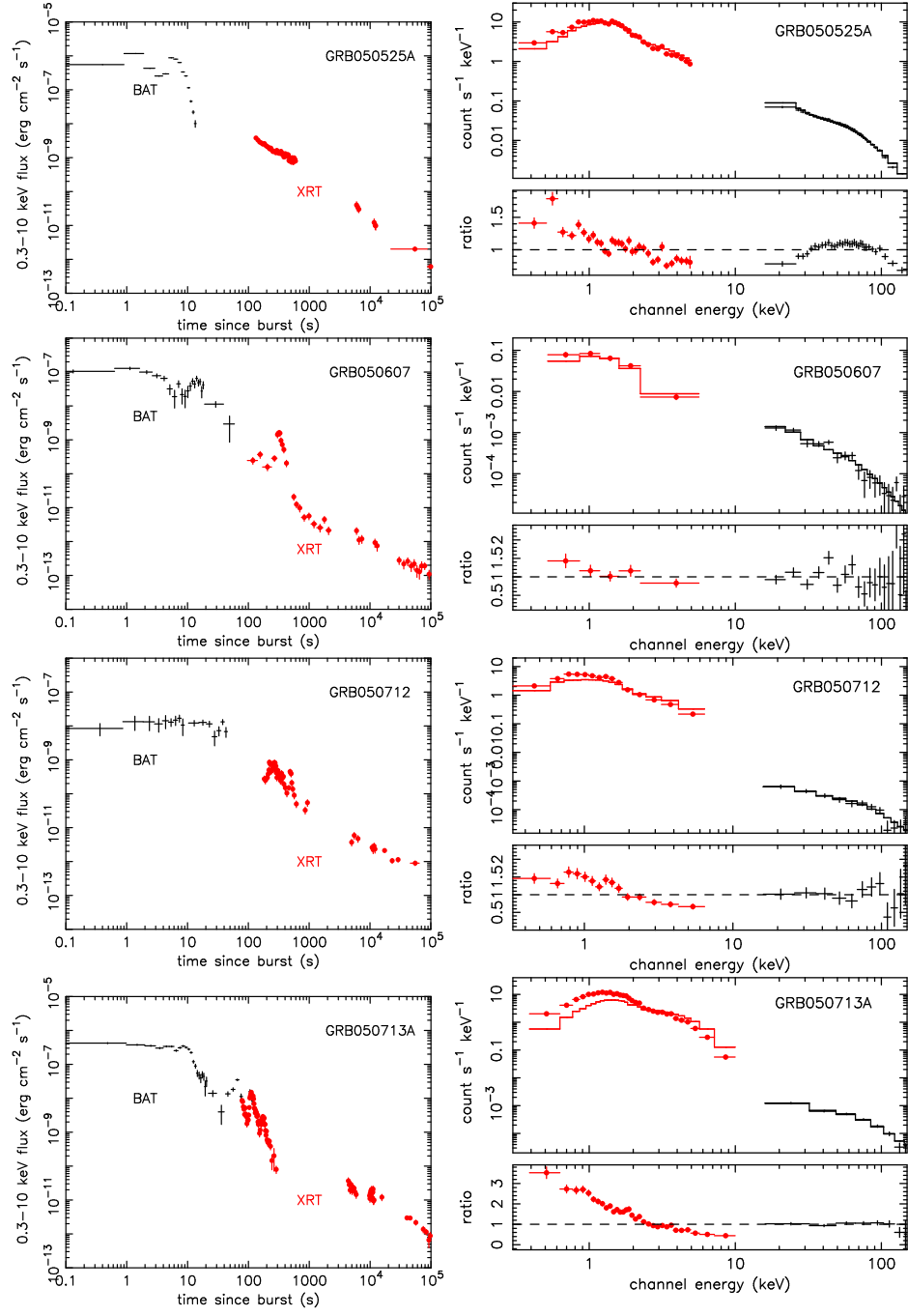


Fig. 2. — continued.

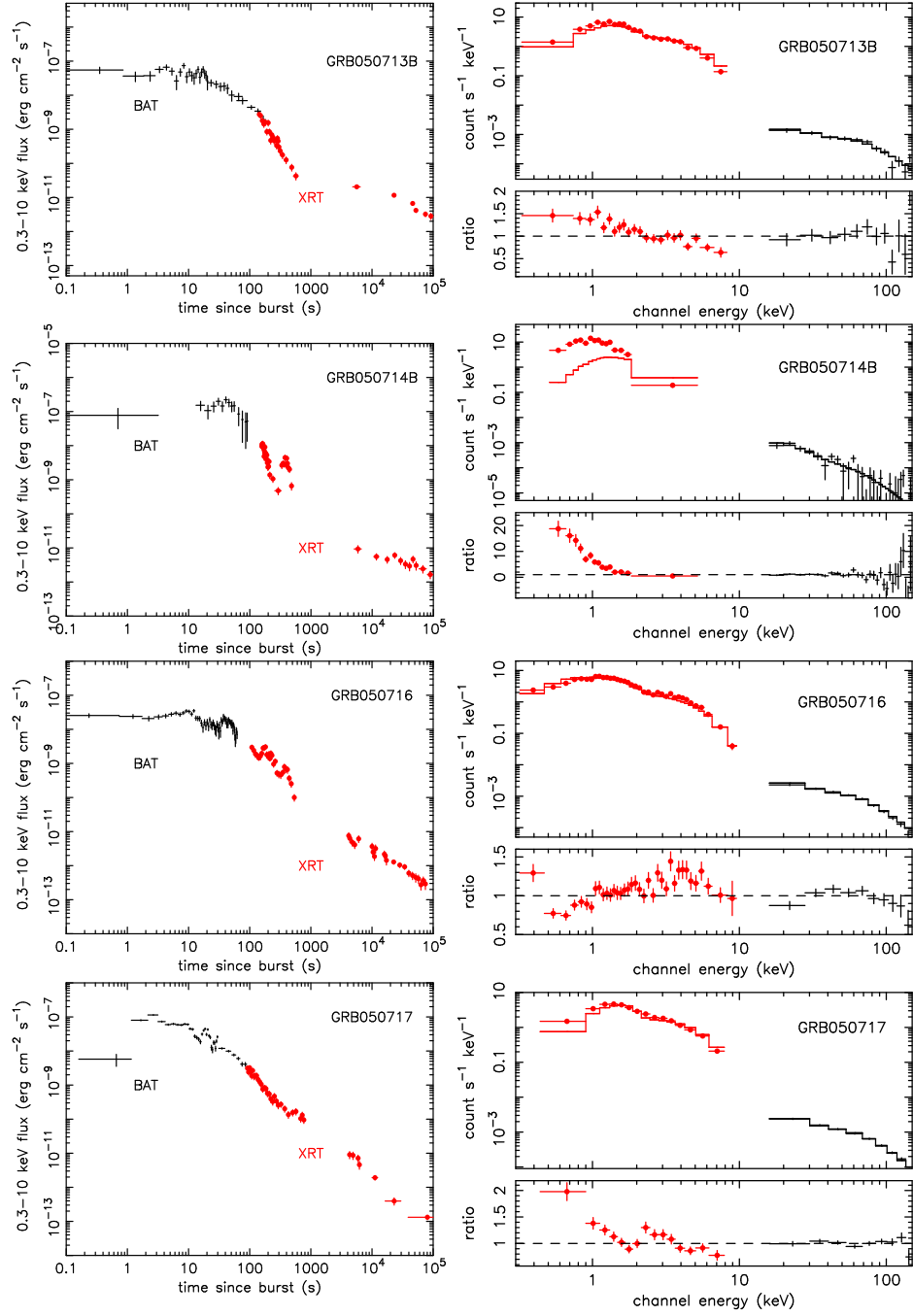


Fig. 2. — continued.

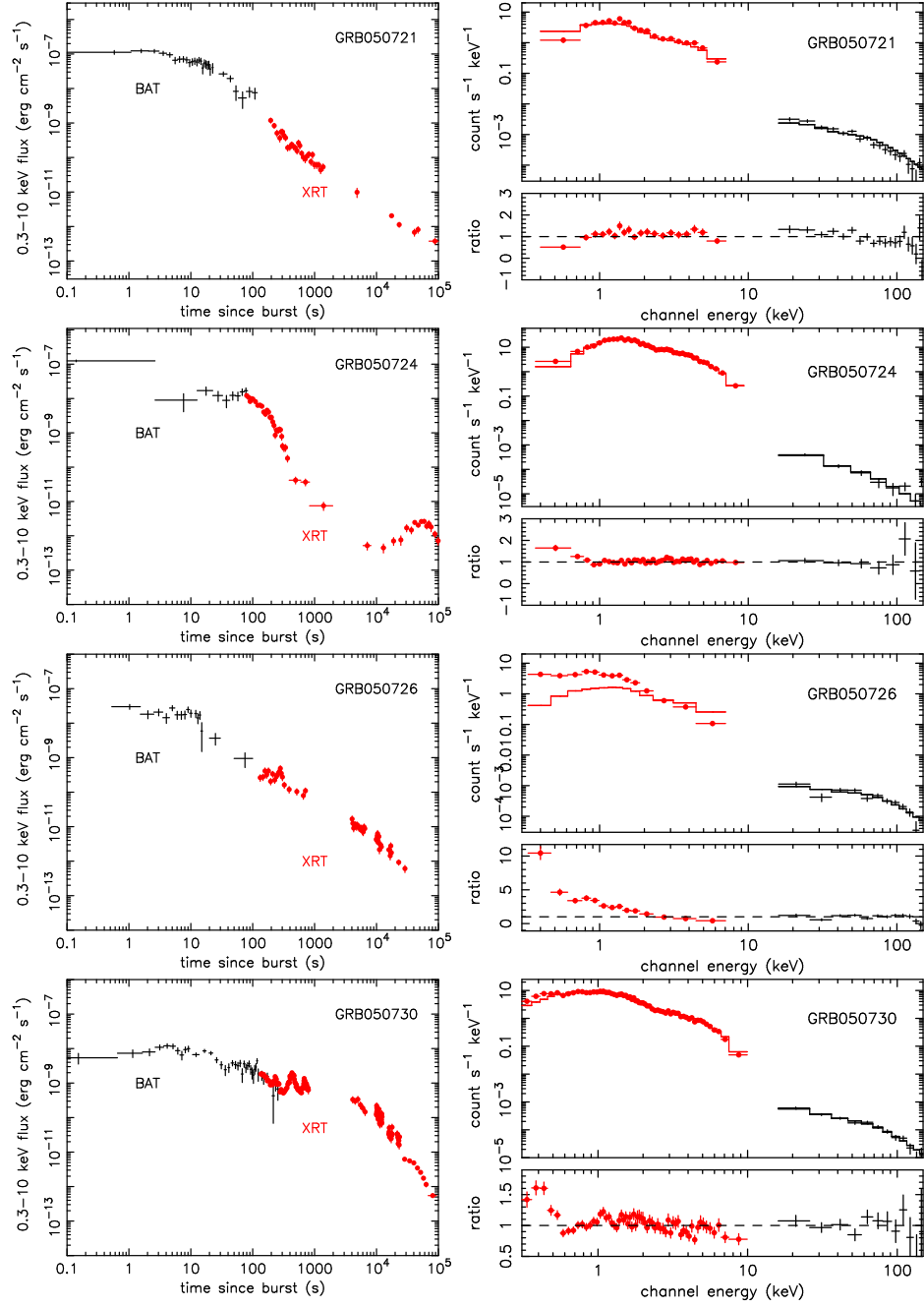


Fig. 2. — continued.

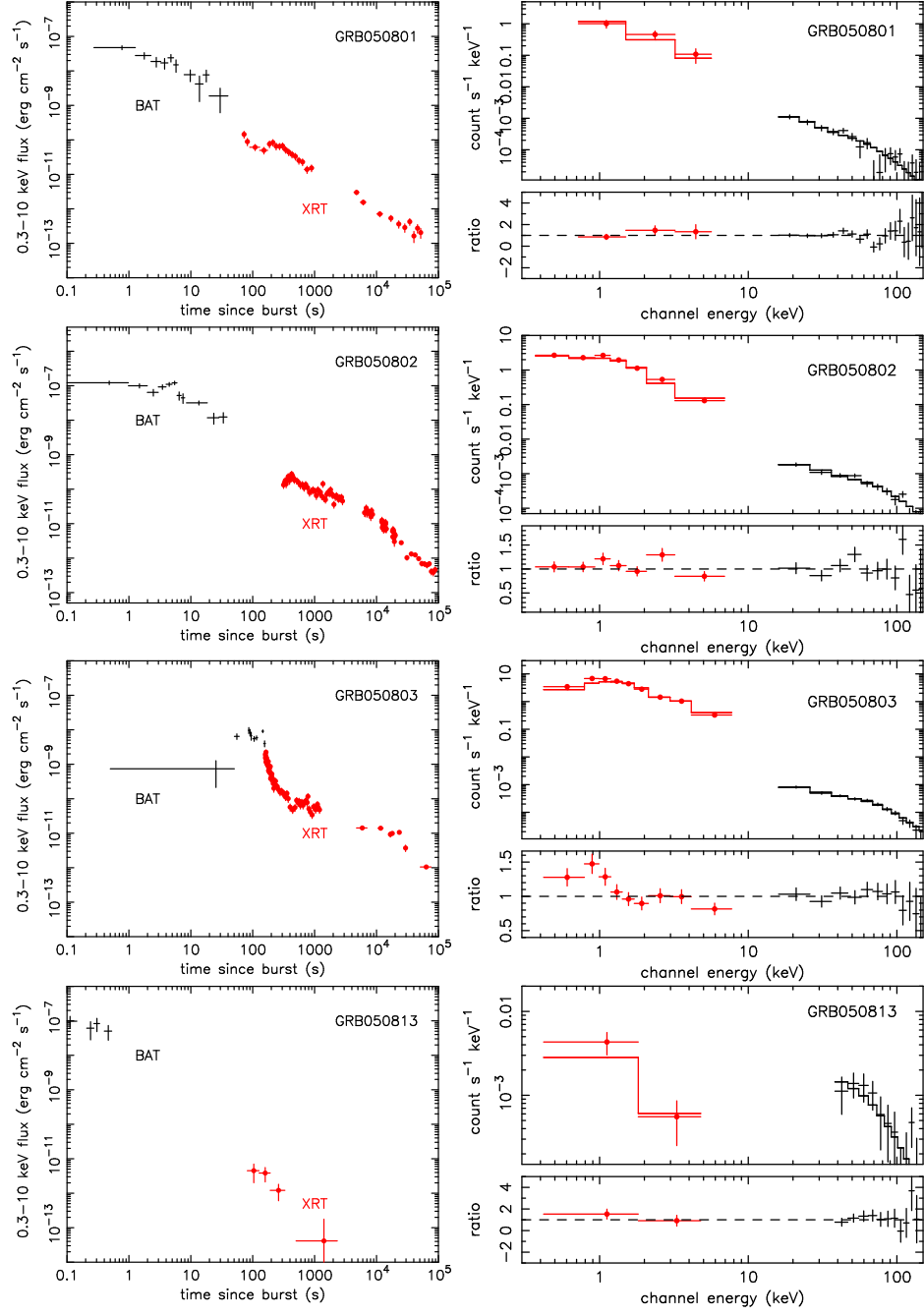


Fig. 2. — continued.

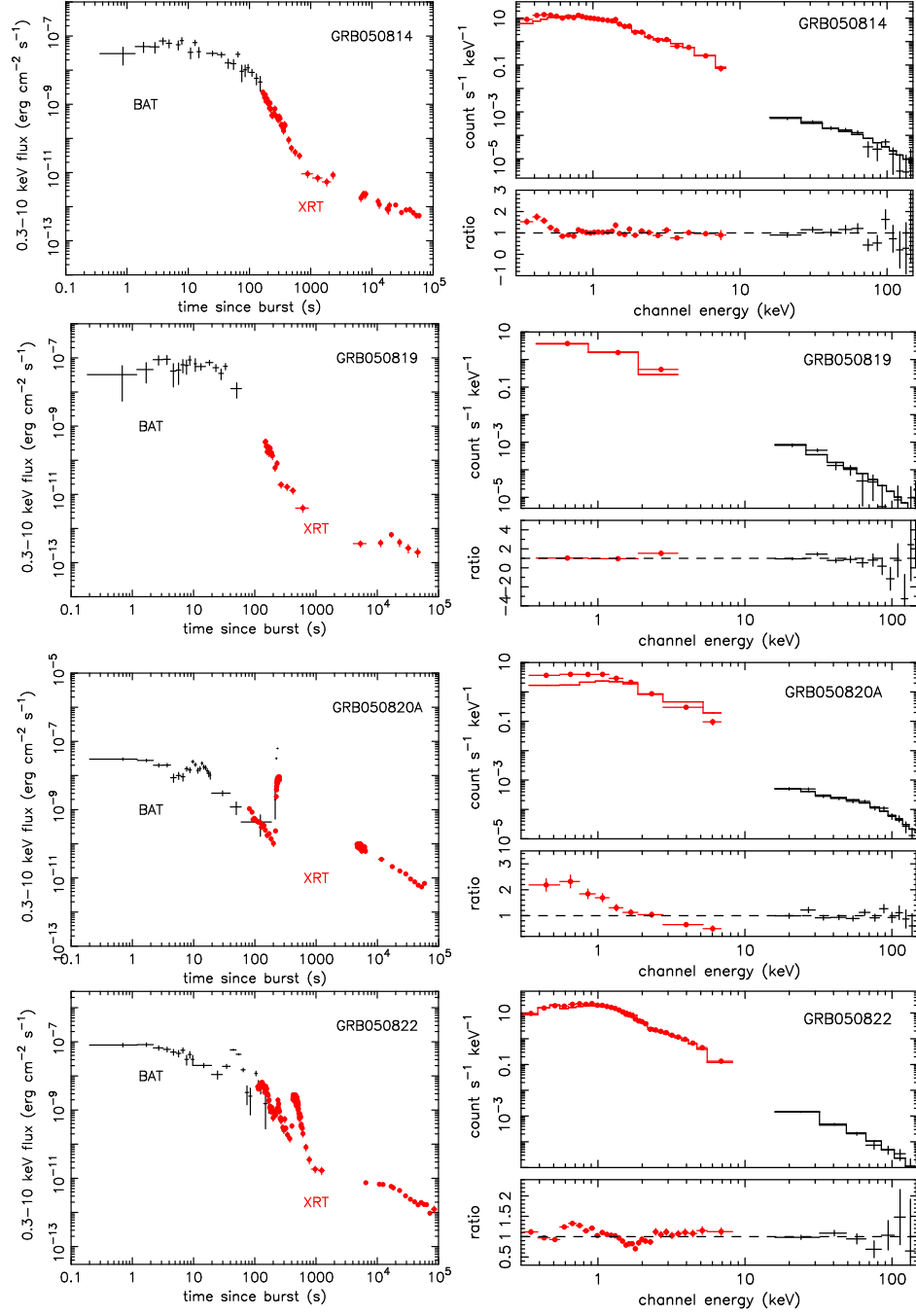


Fig. 2. — continued.



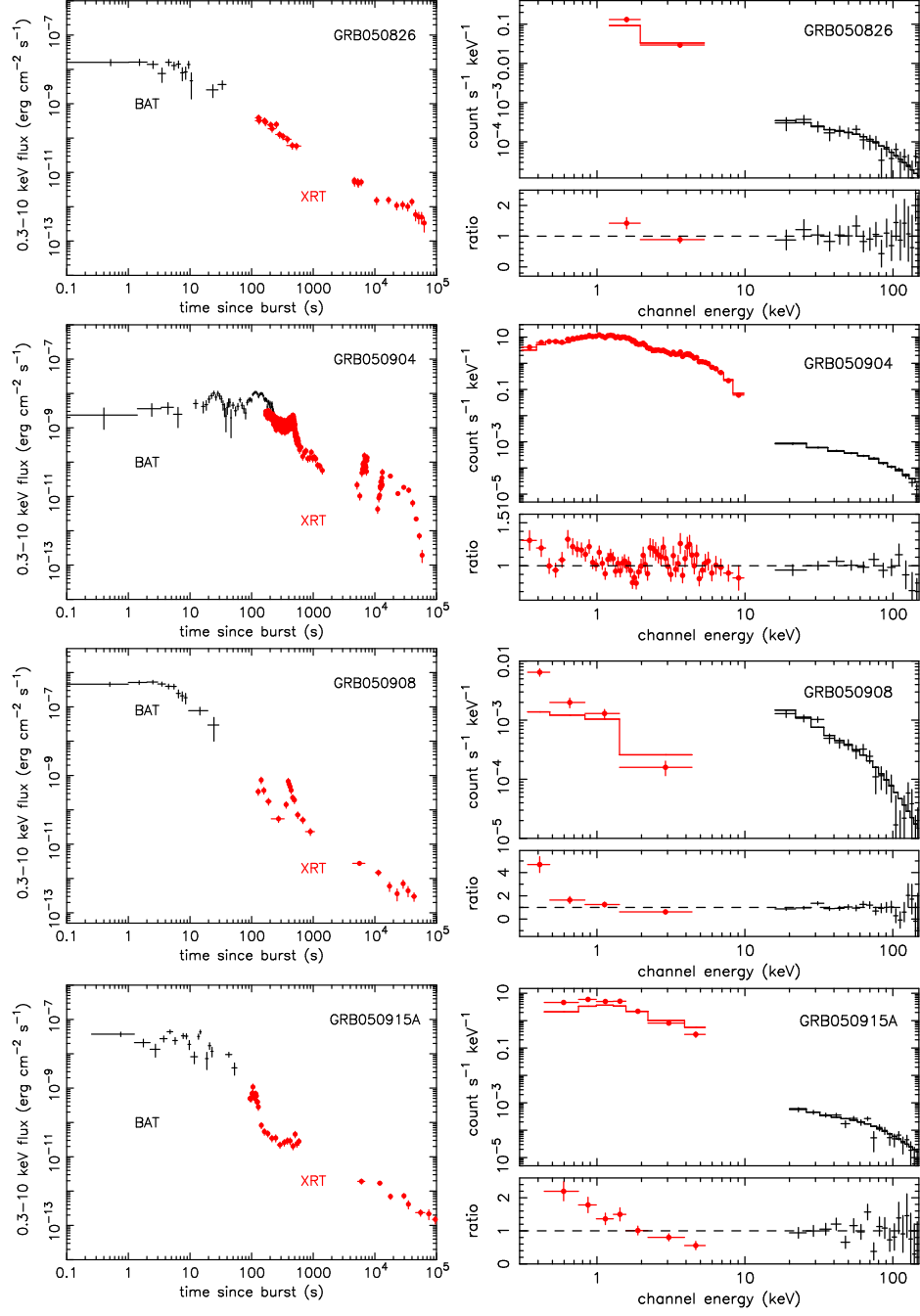


Fig. 2. — continued.

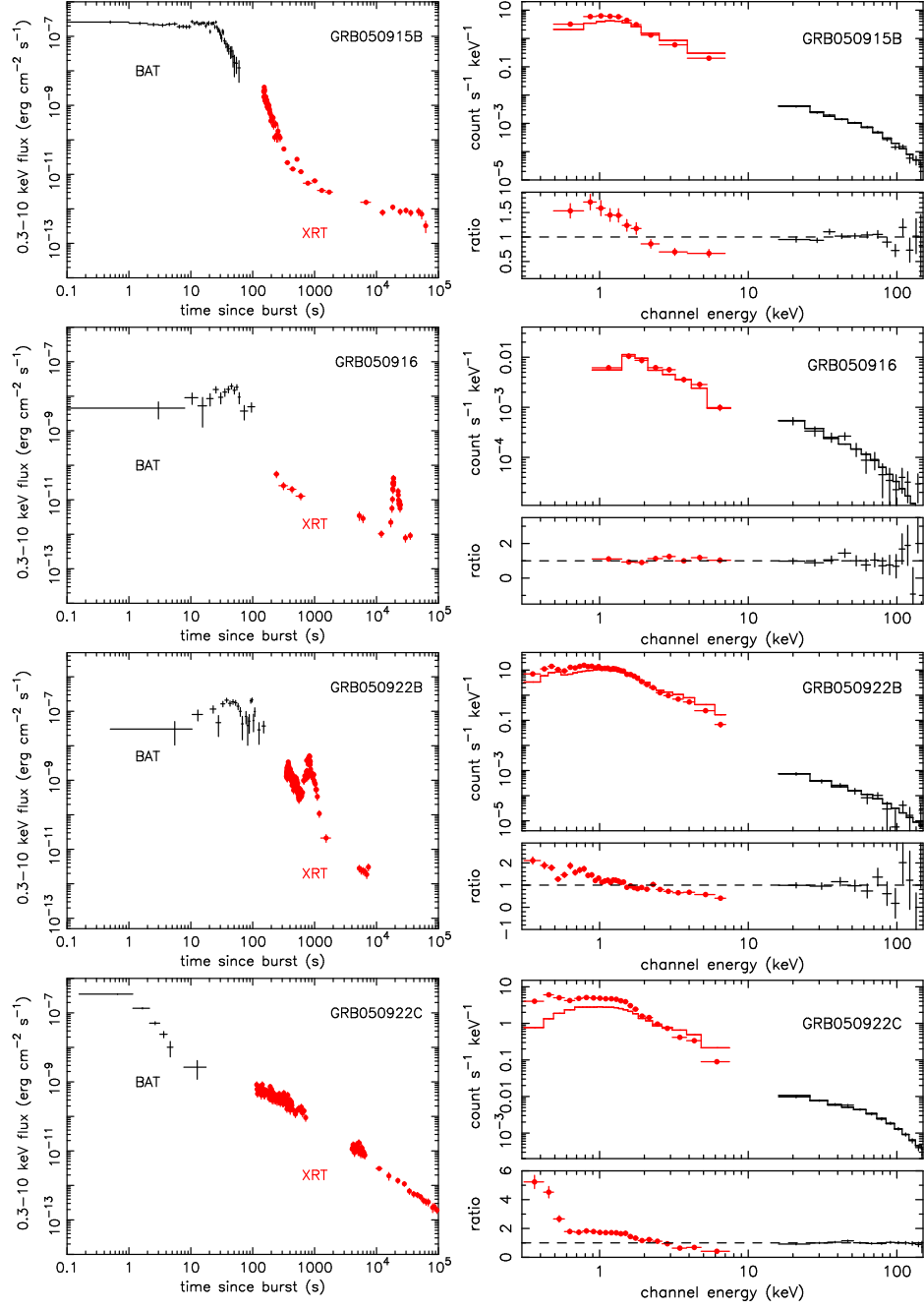


Fig. 2. — continued.

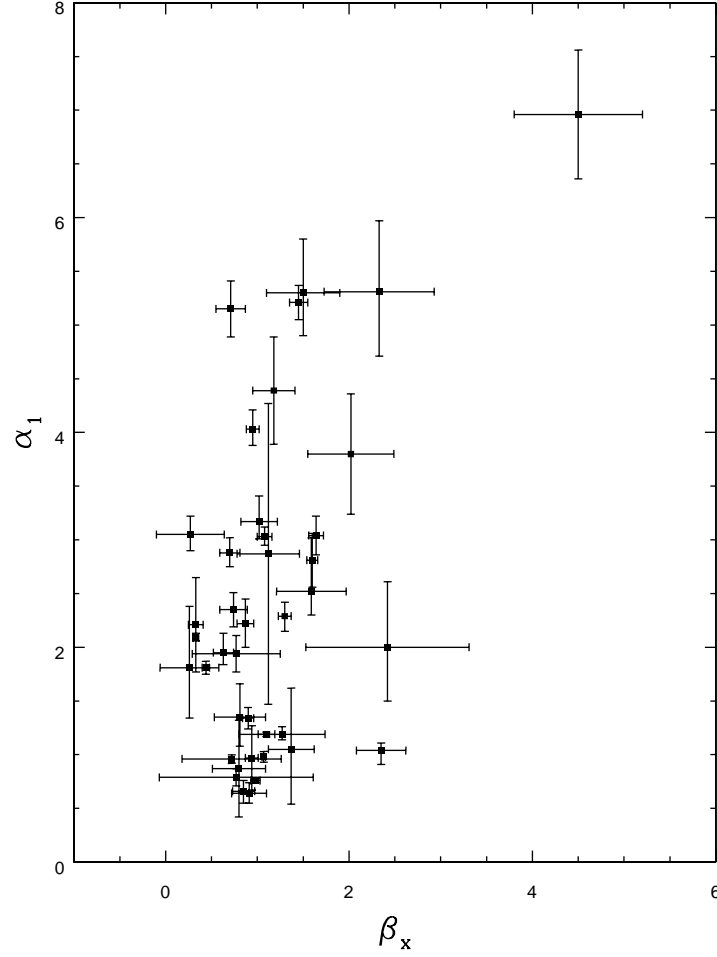


Fig. 3.— The relationship between the observed X-ray temporal ( $\alpha_1$ ) and spectral ( $\beta_x$ ) indices. The outlier at top-right is GRB050714B.

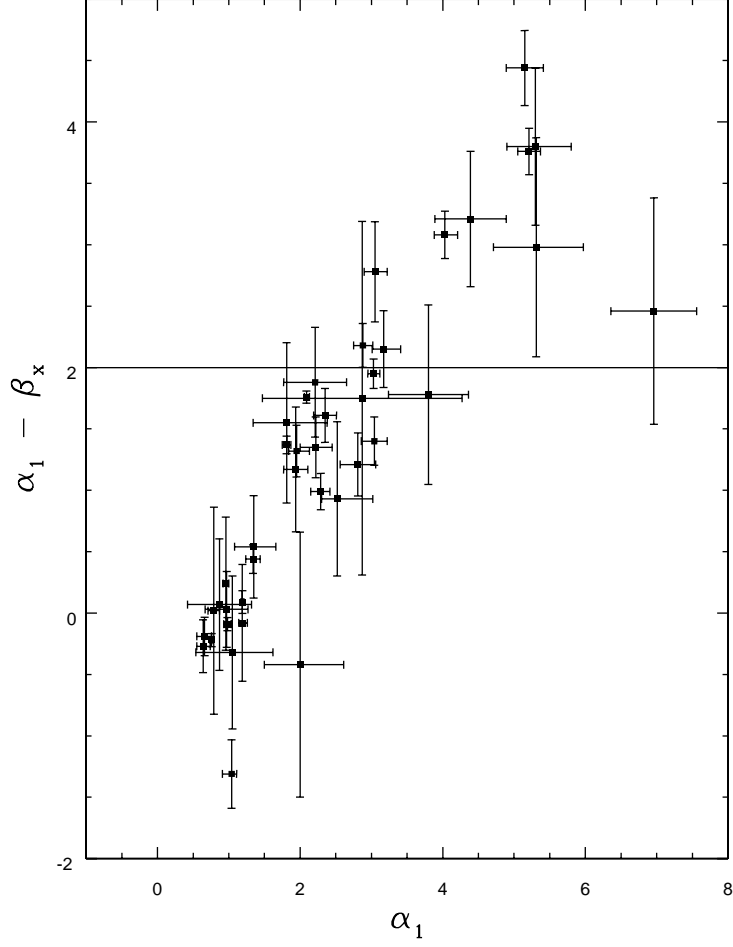


Fig. 4.— The difference between the observed X-ray temporal ( $\alpha_1$ ) and spectral ( $\beta_x$ ) indices, derived from the early XRT data, as a function of temporal index. The horizontal line shows  $\alpha_1 - \beta_x = 2$  as predicted by the high latitude emission model (Kumar & Panaitescu 2000).

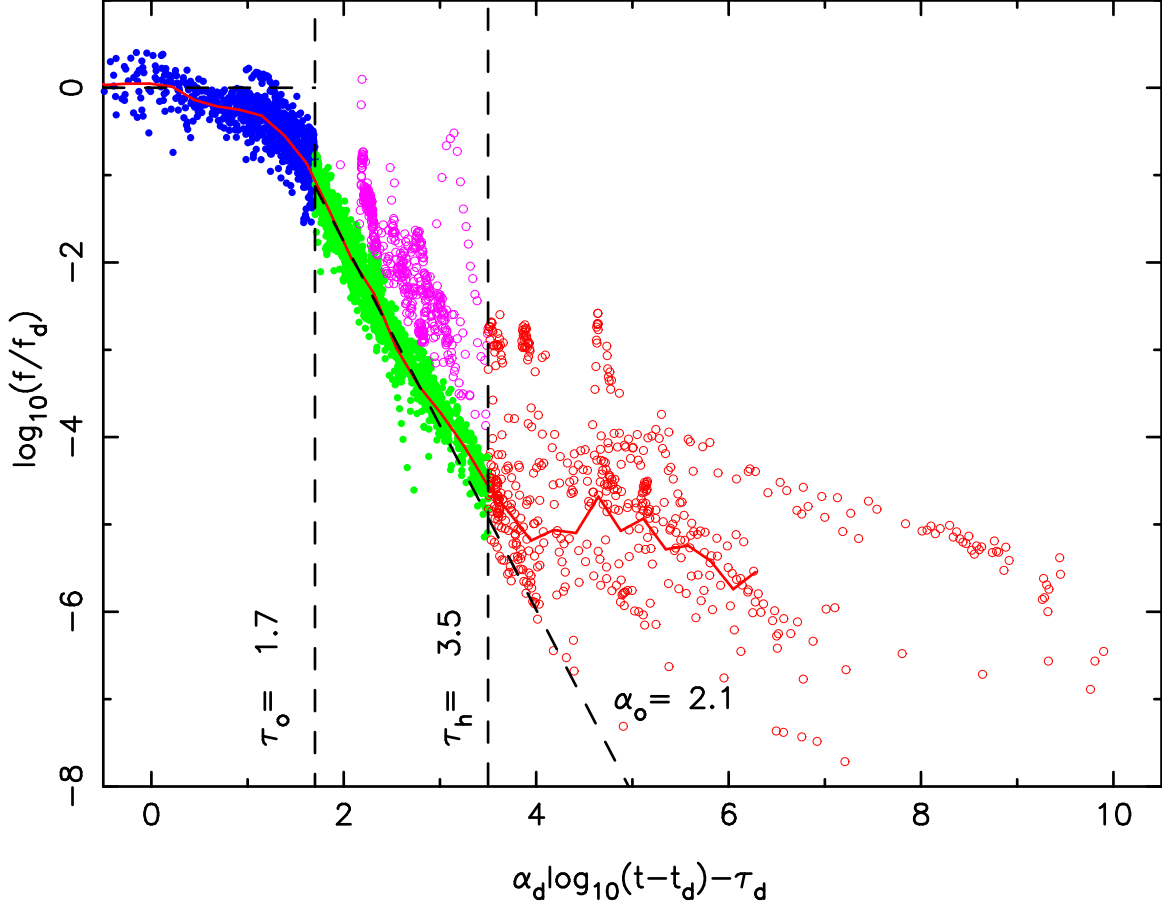


Fig. 5.— Composite decay curve derived from 40 GRBs. See text for details. The filled (blue) circles at  $\tau < 1.7$  are within time  $T_p$ . The average produced by the least squares procedure is shown as the solid (red) line. The dashed power law slope indicates the best fit to the initial decay in the average curve derived using the filled (green) circles. The open circles indicate flux measurements which were excluded from the power law fitting as flares (pink) or because  $\tau > 3.5$  (red).

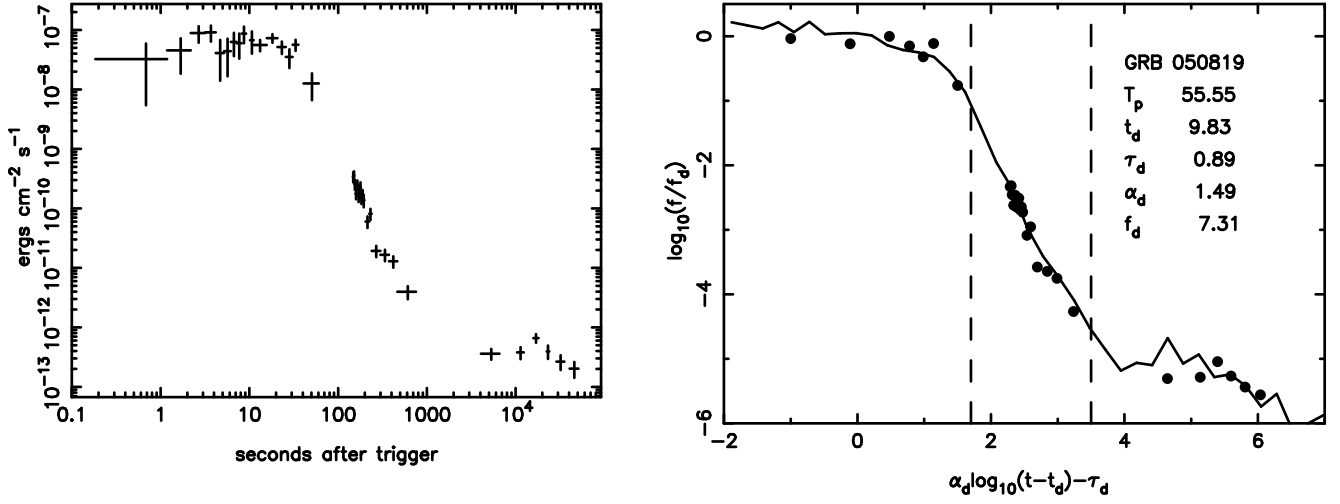


Fig. 6.— Left-hand panel: The unabsorbed 0.3–10 keV flux light curve for GRB 050819. Right-hand panel: transformed light curve with best fit parameters. Vertical lines and solid curve as in Fig. 5.

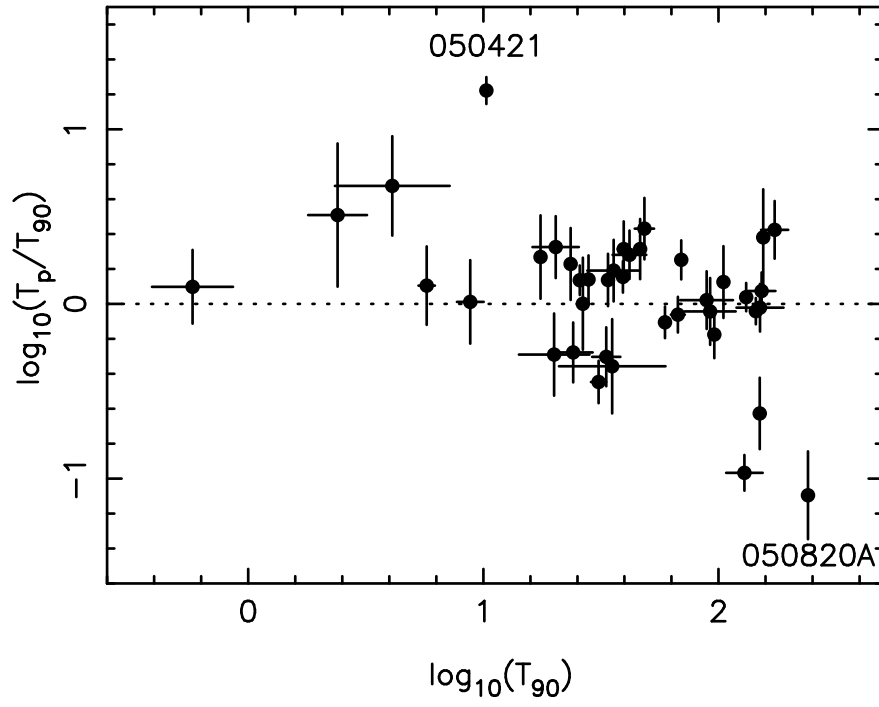


Fig. 7.— The prompt time  $T_p$  compared with  $T_{90}$ .

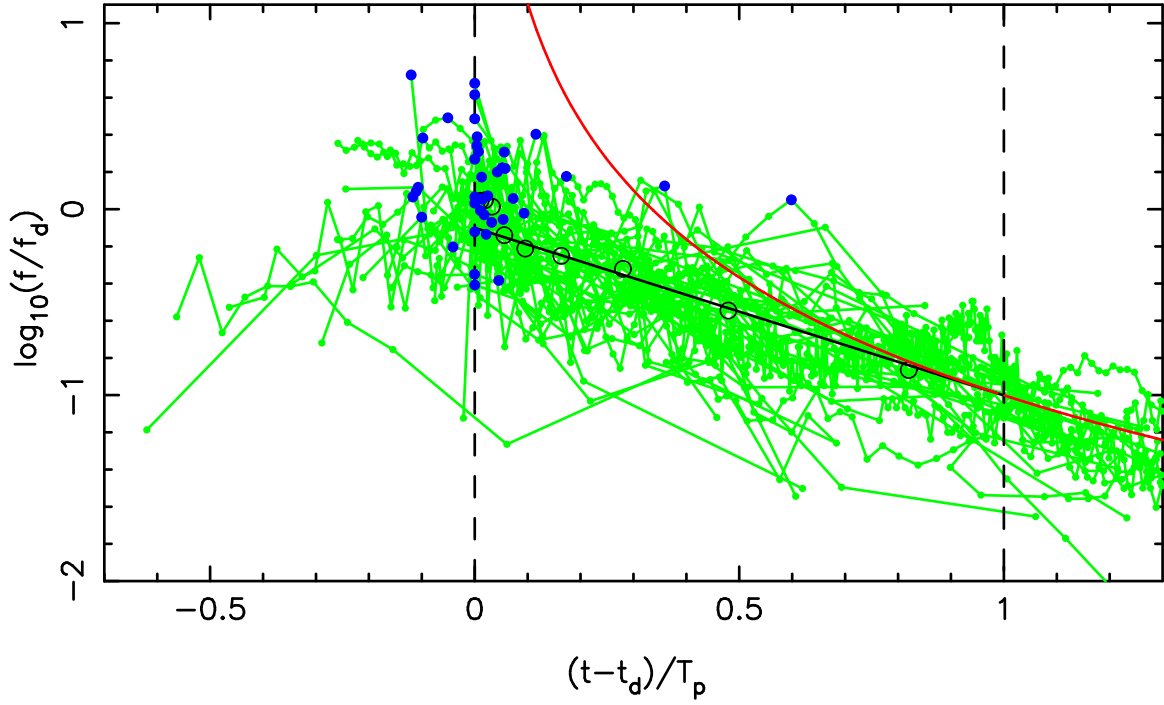


Fig. 8.— The distribution of peak flux times (filled (blue) circles) about time zero produced by the least-squares fitting. The connected open circles show the average decay curve relative to the individual (green) light curves plotted in linear time relative to  $T_p$ . The curved (red) solid line shows the backwards extrapolation of the average power law which fits times above  $T_p$ . The vertical dashed lines correspond to 0 and  $T_p$ .



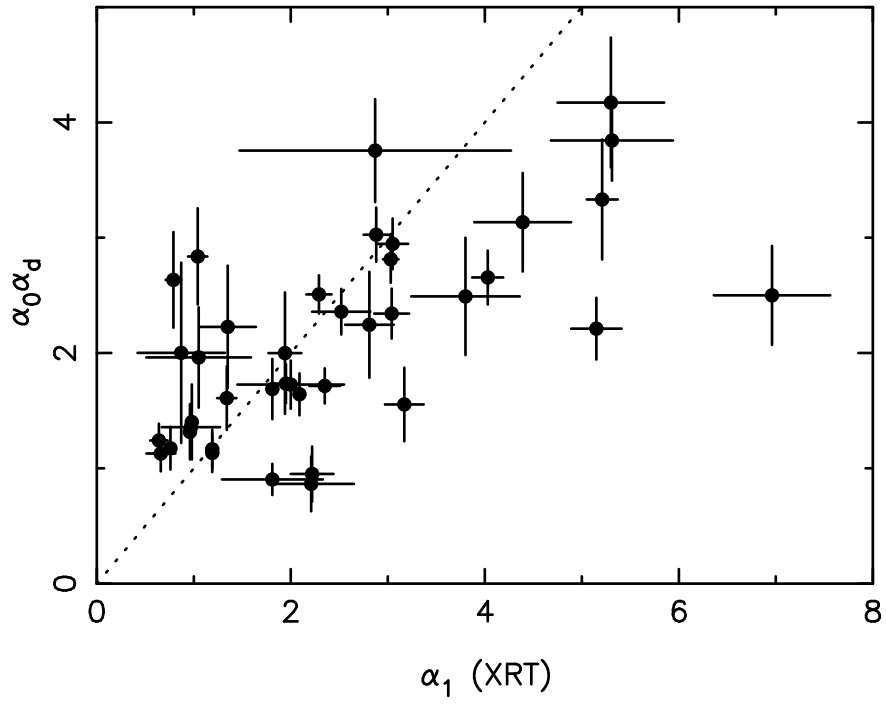


Fig. 9.— Correlation of  $\alpha_0 \alpha_d$  derived from the global light curve fit with  $\alpha_1$  estimated from the XRT light curve. The dotted line shows  $\alpha_0 \alpha_d = \alpha_1$ .

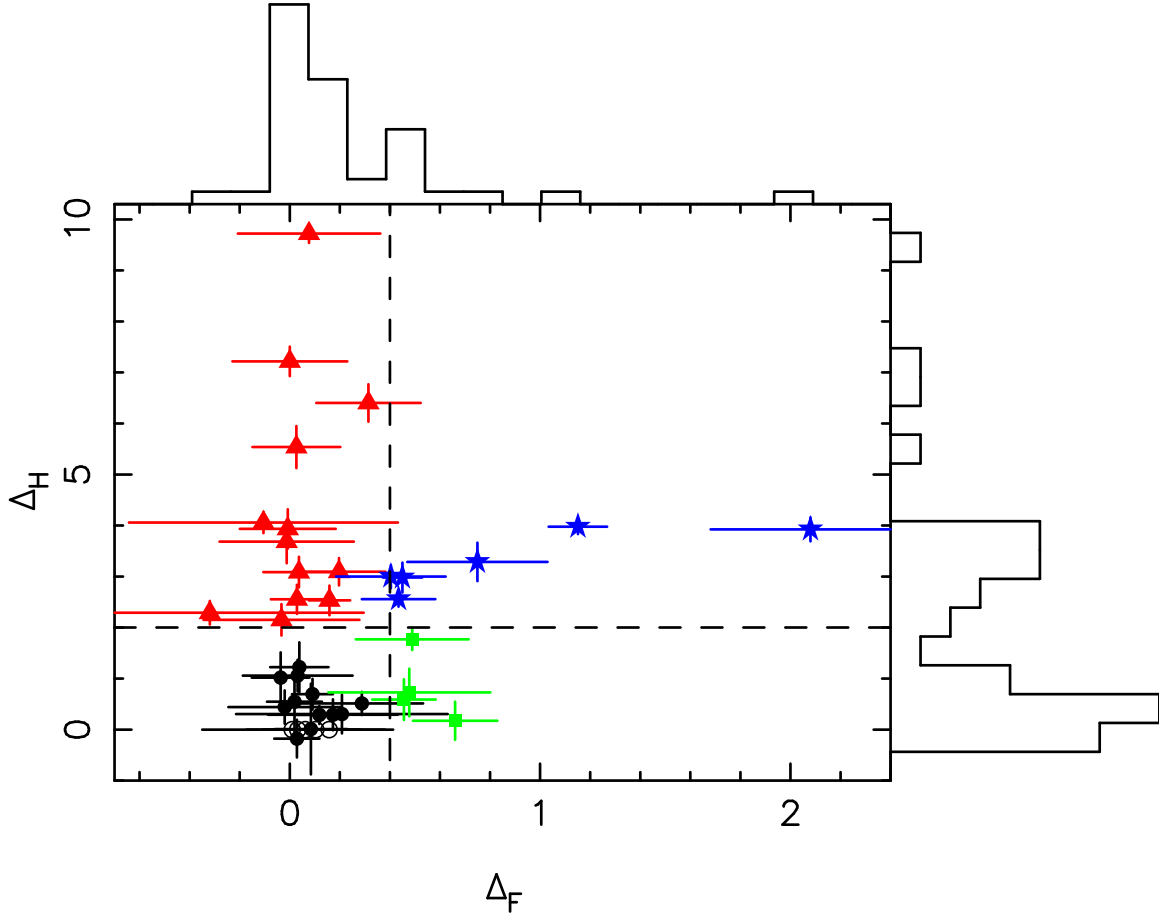


Fig. 10.— The distribution of  $\Delta_F$  (measure of flaring activity) and  $\Delta_H$  (measure of size of late hump). The GRBs in each quadrant are shown as filled (black) circles (no significant flares or hump), filled (green) squares (flares but no hump), filled (blue) stars (flares and hump) and filled (red) triangles (hump but no flares). The open circles denote GRBs for which there are no data in the light curve with  $\tau > 3.5$ .

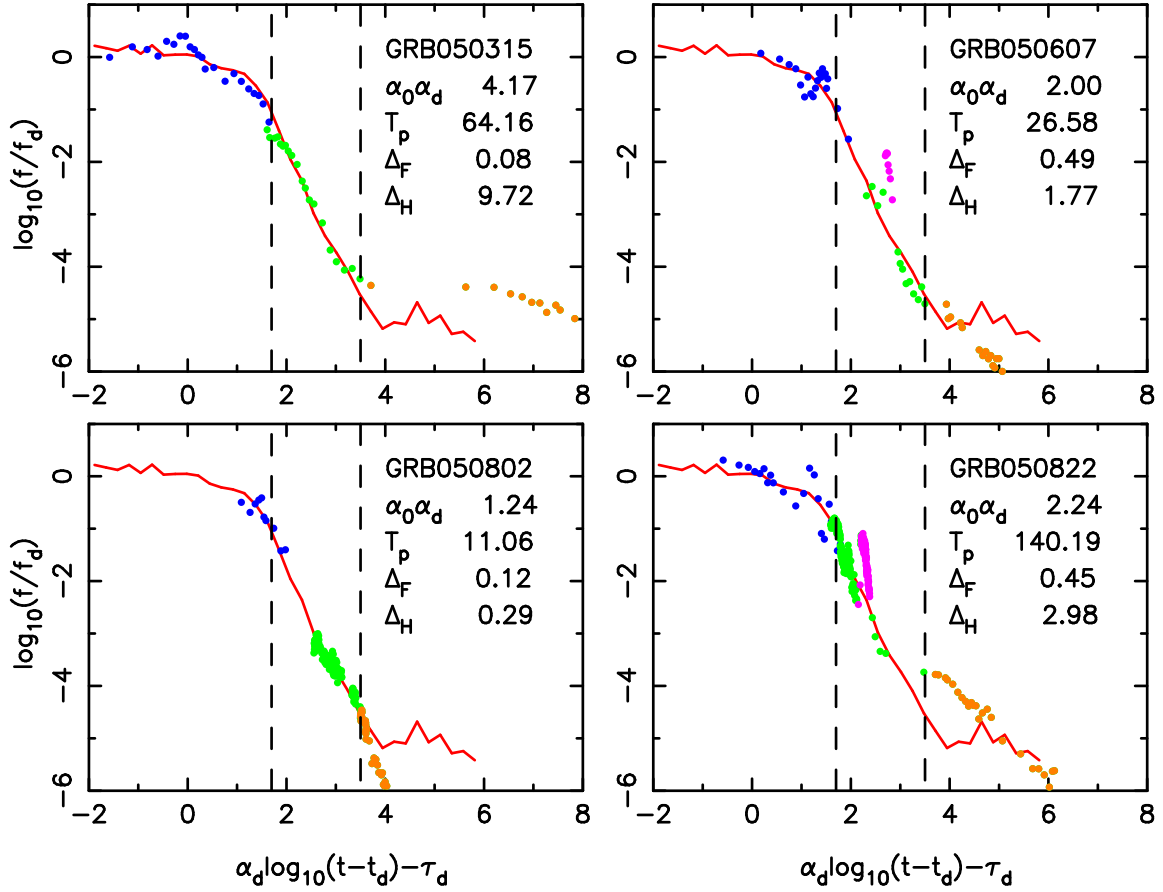


Fig. 11.— Examples of scaled GRB light curves fitted to the average decay curve. Top-left panel: No flares with prominent late hump. Top-right panel: Flares with weak late hump. Bottom-left panel: No flares or late hump. Bottom-right panel: Prominent flares and moderate late hump. BAT data are filled blue circles, XRT data are filled green circles. Flares and hump are filled purple and orange circles respectively. Vertical dashed lines as in Fig. 5.

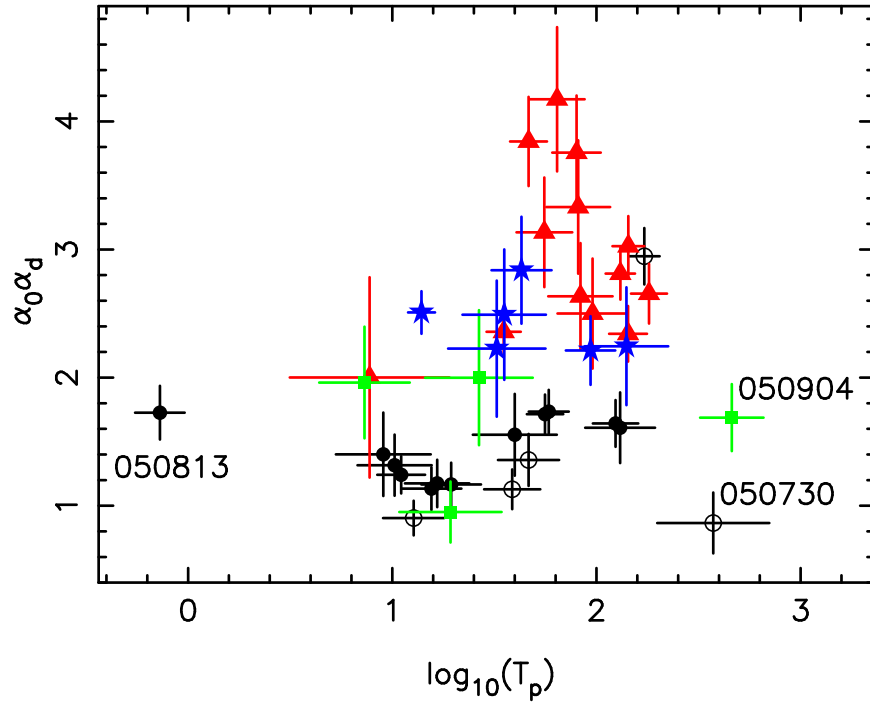


Fig. 12.— Distribution of  $\alpha_0 \alpha_d$  and  $\log_{10}(T_p)$ . Symbols as in Fig. 10.

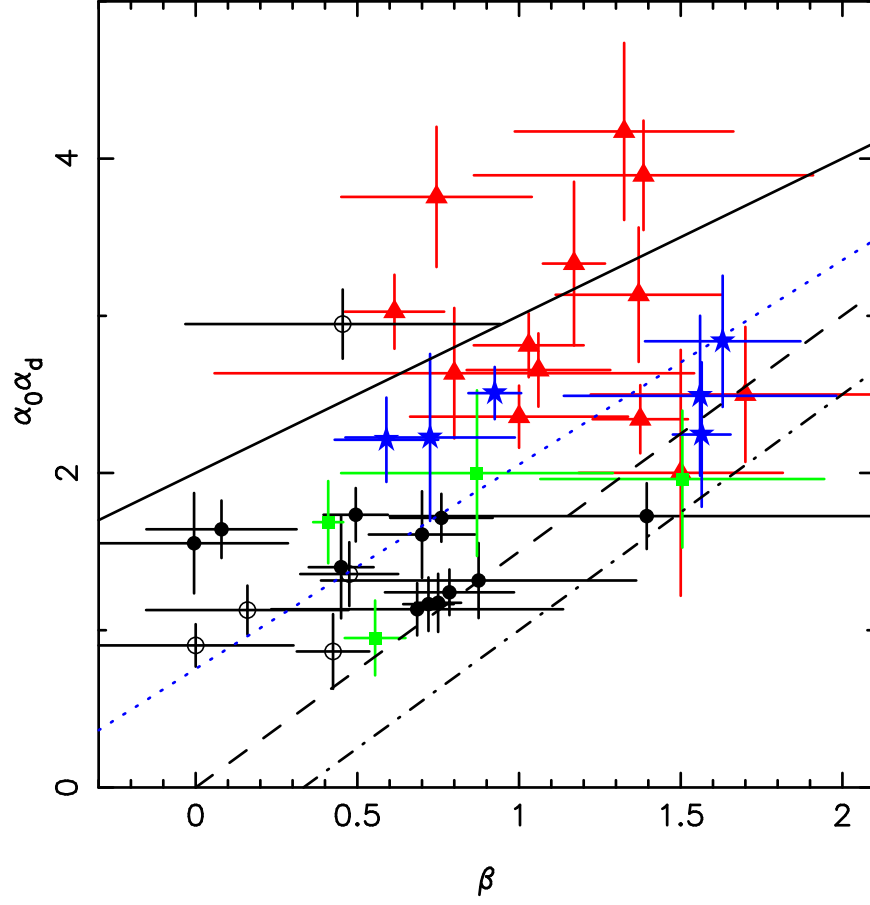


Fig. 13.— Correlation of  $\alpha_0\alpha_d$  with  $\beta$ , where  $\beta$  is the average of the spectral indices from the BAT and XRT. Symbols as in Fig. 10. The solid diagonal line shows the predictions of the high latitude model. The dashed and dot-dashed diagonal lines show the two afterglow models discussed in the text. The dotted diagonal line shows a fit to those bursts below the high latitude line.

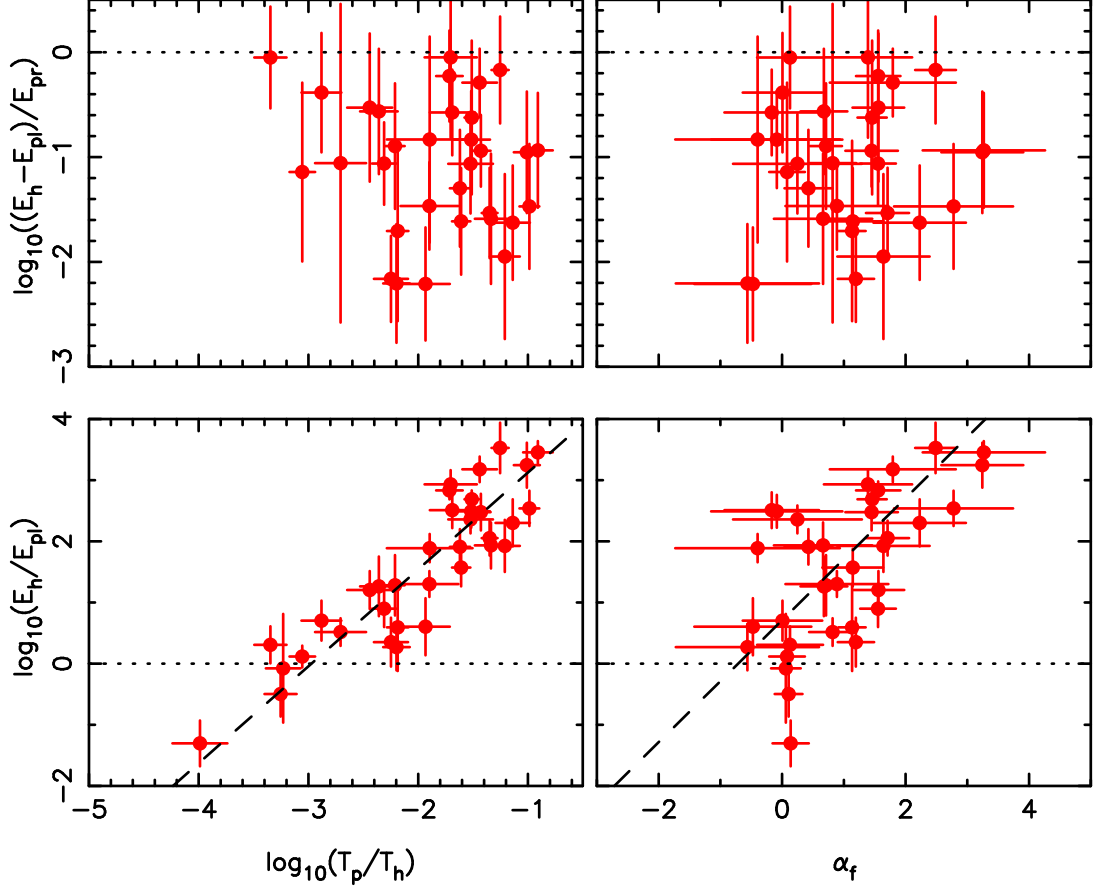


Fig. 14.— Bottom panels: The ratio of the size of the late hump emission to the power law,  $E_h/E_{pl}$ , compared with  $T_p/T_h$  and  $\alpha_f$ . The horizontal dotted line corresponds to equal fluence in both. Top panels: The ratio of the fluence in the late hump emission to that of the prompt,  $(E_h - E_{pl})/E_{pr}$ , compared with  $T_p/T_h$  and  $\alpha_f$ . The horizontal dotted line corresponds to equal fluence in both.

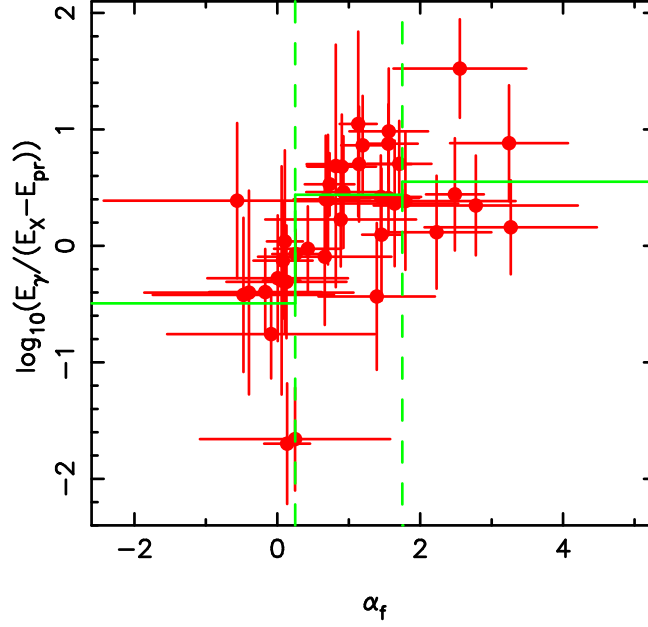


Fig. 15.— Comparison of the hard prompt fluence,  $E_\gamma$  (15–150 keV) for  $t < T_p$ , with the soft X-ray decay fluence,  $E_X - E_{pr}$  (0.3–10 keV) for  $t > T_p$ . The vertical dashed lines correspond to  $\alpha_f = 0.25$  and  $1.75$  respectively (see text).

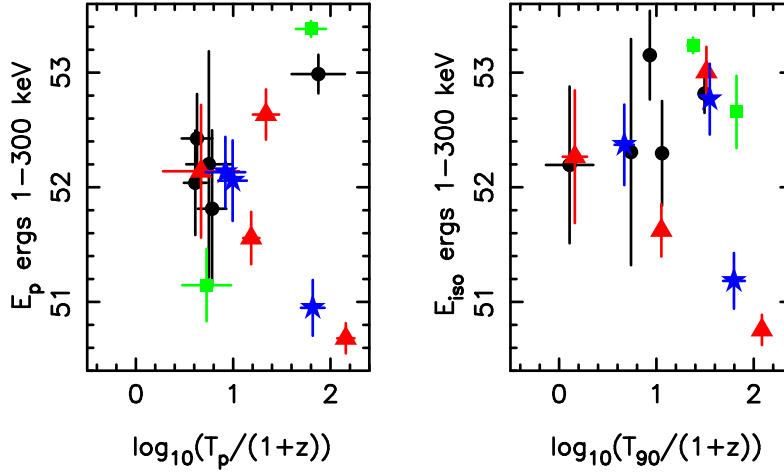


Fig. 16.— Left-hand panel: Isotropic equivalent energy in the hard prompt emission,  $E_p$  (1–300 keV) for  $t < T_p$ , calculated for those bursts for which we have a redshift. Right-hand panel: Corresponding isotropic equivalent energy in the 1–300 keV band derived over  $T_{90}$ . Symbols as in Fig. 10.